

## Iso-vector axial form factors of the nucleon in two-flavour lattice QCD

S. Capitani,<sup>1,2,3</sup> M. Della Morte,<sup>4</sup> D. Djukanovic,<sup>1,2,\*</sup> G.M. von Hippel,<sup>1,†</sup> J. Hua,<sup>1,2</sup>  
 B. Jäger,<sup>4,5,6</sup> P.M. Junnarkar,<sup>2,7</sup> H.B. Meyer,<sup>1,2,‡</sup> T.D. Rae,<sup>1</sup> and H. Wittig<sup>1,2,§</sup>

<sup>1</sup>*PRISMA Cluster of Excellence and Institut für Kernphysik,  
 University of Mainz, Johann-Joachim-Becher-Weg 45, 55099 Mainz, Germany*

<sup>2</sup>*Helmholtz Institute Mainz, University of Mainz, 55099 Mainz, Germany*

<sup>3</sup>*Institut für Theoretische Physik, Goethe-Universität Frankfurt,  
 Max-von-Laue-Str. 1, 60438 Frankfurt am Main, Germany*

<sup>4</sup>*CP<sup>3</sup>-Origins & Danish IAS, University of Southern Denmark, Campusvej 55, 5230 Odense M, Denmark*

<sup>5</sup>*Department of Physics, College of Science, Swansea University, Swansea SA2 8PP, United Kingdom*

<sup>6</sup>*ETH Zürich, Institute for Theoretical Physics, Wolfgang-Pauli-Str. 27, 8093 Zürich, Switzerland*

<sup>7</sup>*Tata Institute of Fundamental Research (TIFR), Homi Bhabha Rd., 400005 Mumbai, India*

We present a lattice calculation of the nucleon iso-vector axial and induced pseudoscalar form factors on the CLS ensembles using  $N_f = 2$  dynamical flavours of non-perturbatively  $\mathcal{O}(a)$ -improved Wilson fermions and an  $\mathcal{O}(a)$ -improved axial current together with the pseudoscalar density. Excited-state effects in the extraction of the form factors are treated using a variety of methods, with a detailed discussion of their respective merits. The chiral and continuum extrapolation of the results is performed both using formulae inspired by Heavy Baryon Chiral Perturbation Theory (HBChPT) and a global approach to the form factors based on a chiral effective theory (EFT) including axial vector mesons. Our results indicate that careful treatment of excited-state effects is important in order to obtain reliable results for the axial form factors of the nucleon, and that the main remaining error stems from the systematic uncertainties of the chiral extrapolation. As final results, we quote  $g_A = 1.278 \pm 0.068^{+0.000}_{-0.087}$ ,  $\langle r_A^2 \rangle = 0.360 \pm 0.036^{+0.080}_{-0.088}$  fm<sup>2</sup>, and  $g_P = 7.7 \pm 1.8^{+0.8}_{-2.0}$  for the axial charge, axial charge radius and induced pseudoscalar charge, respectively, where the first error is statistical and the second is systematic.

PACS numbers: 12.38.Gc, 14.20.Dh

Keywords: nucleon form factors; nucleon axial charge; lattice QCD

arXiv:1705.06186v4 [hep-lat] 30 Jan 2019

---

\* [d.djukanovic@him.uni-mainz.de](mailto:d.djukanovic@him.uni-mainz.de)

† [hippel@uni-mainz.de](mailto:hippel@uni-mainz.de)

‡ [meyerh@uni-mainz.de](mailto:meyerh@uni-mainz.de)

§ [wittig@uni-mainz.de](mailto:wittig@uni-mainz.de)

## I. INTRODUCTION

The structure of the nucleon is of fundamental importance in characterizing matter at subatomic length scales. Nucleon structure can be studied experimentally using the electroweak gauge bosons ( $\gamma$ ,  $Z$ ,  $W^\pm$ ) as probes. In many cases, these interactions must be understood quantitatively in order to interpret precision experiments searching for new physics.

The interaction of an electroweak gauge boson with the nucleon is parameterized by form factors. Specifically, the photon couples via the electromagnetic current, while the  $W^\pm$  boson couples to the left-handed component  $\bar{q}\gamma_\mu(1-\gamma_5)q$  of the quarks with weak-isospin charge factors. While the electromagnetic form factors are well determined, the matrix elements of the axial current  $\bar{q}\gamma_\mu\gamma_5q$  are less precisely known. Focusing on the light-quark contribution, the nucleon matrix elements of the iso-vector axial current are encoded in the axial and induced pseudoscalar form factors. The axial charge of the nucleon, defined as the axial form factor at zero momentum transfer, can be interpreted as the fractional contribution from quark and antiquark spins to the nucleon spin and is known experimentally to an accuracy of two parts per mille through neutron beta-decay processes [1]. The momentum-transfer dependence of the axial form factor, which can be related to the transverse densities of helicity-aligned minus anti-aligned quarks and antiquarks in the infinite-momentum frame [2], is much less well known. A recent analysis [3] assigns an uncertainty of about twenty percent to the axial charge radius, which is given by the slope of the axial form factor at  $Q^2 = 0$  (see Eq. (4) below). The axial form factor is accessible primarily via neutrino scattering off the nucleon [3–5], and, at low momentum transfer, via the electro-production of charged pions [6, 7]. There is a tension between the values of the axial radius  $\langle r_A^2 \rangle$  obtained by these two experimental techniques [8]. The induced pseudoscalar form factor, which is related to the pion-nucleon form factor through the Goldberger-Treiman relation [9, 10], is measured experimentally in muon-capture processes on the proton [11, 12] and has recently been determined at the seven percent level [13, 14].

Lattice QCD determinations of nucleon form factors have a long tradition [15]. They are based on evaluating two- and three-point functions in four-dimensional Euclidean space in the path integral formalism with the help of importance-sampling Monte-Carlo techniques. Calculations of the nucleon axial charge [16–28] have tended to yield lower values than the experimental one at physical quark masses. This is widely believed to be due to a failure to properly account for excited-state contributions in the lattice simulations [18, 29, 30], although lattice cutoff effects, finite-size effects [16, 19] and even finite-temperature effects [17] must be kept under control as well. Lattice studies of the momentum dependence of the axial form factors are not as numerous yet, but have become more common recently [31–38]. Since the axial form factor of the nucleon is an important source of uncertainty in determining the neutrino flux in long-baseline neutrino experiments [3, 39], an accurate QCD prediction from the lattice is now particularly timely.

This paper is structured as follows: we describe our general lattice setup in section II, and give details on our treatment of the excited-state contaminations in section III. Our results for the axial form factor are presented in section IV, and for the induced pseudoscalar form factor in section V. We discuss different ways of performing the chiral and continuum extrapolation of our results in section VI, and conclude with a discussion of our findings and their implications in section VII.

A complete set of our results for the form factors on all lattice ensembles used is given in A.

## II. LATTICE SET-UP

### A. Observables and correlators

We employ a Euclidean notation throughout. The matrix element of the local iso-vector axial current  $A_\mu^a(x) = \bar{\psi}\gamma_\mu\gamma_5\frac{\tau^a}{2}\psi$  between single-nucleon states can be parameterised by the axial form factor  $G_A(Q^2)$  and induced pseudoscalar form factor  $G_P(Q^2)$  as

$$\begin{aligned} \langle N(p', s') | A_\mu^a(0) | N(p, s) \rangle = \\ \bar{u}(p') \left( \gamma_\mu \gamma_5 G_A(Q^2) - i \gamma_5 \frac{Q_\mu}{2M_N} G_P(Q^2) \right) \frac{\tau^a}{2} u(p), \end{aligned} \quad (1)$$

where  $Q_\mu = (iE_{p'} - iE_p, \mathbf{q})$ ,  $\mathbf{q} = \mathbf{p}' - \mathbf{p}$ ,  $u(p)$  is an isodoublet Dirac spinor with momentum  $p$ ,  $\gamma_\mu$  is a Dirac matrix, and  $M_N$  is the nucleon mass. The square of the four-momentum transferred to the nucleon via its interaction with the iso-vector axial current is given by

$$Q^2 = (\mathbf{p}' - \mathbf{p})^2 - (E_{p'} - E_p)^2. \quad (2)$$

In this work, the axial and induced pseudoscalar form factors are computed for space-like momentum transfers  $Q^2 > 0$ . The axial form factor admits a Taylor expansion at low  $Q^2$  given by

$$G_A(Q^2) = g_A \left( 1 - \frac{1}{6} \langle r_A^2 \rangle Q^2 + \mathcal{O}(Q^4) \right), \quad (3)$$

where  $g_A = G_A(Q^2 = 0)$  is the nucleon axial charge and  $\langle r_A^2 \rangle$  is the square of the axial charge radius of the nucleon,

$$\langle r_A^2 \rangle = -\frac{6}{g_A} \left. \frac{\partial G_A(Q^2)}{\partial Q^2} \right|_{Q^2=0}. \quad (4)$$

The pseudoscalar coupling is defined by

$$g_P \equiv \frac{m_\mu}{2m_N} G_P(Q_*^2), \quad (5)$$

with  $Q_*^2 = 0.88m_\mu^2$  the momentum transfer relevant to muon capture with the nucleon at rest [40]. The nucleon matrix element of the iso-vector axial current is related to that of the pseudoscalar current via the chiral Ward identity in two-flavour QCD also known as the partially conserved axial current (PCAC) relation,

$$\partial_\mu A_\mu^a(x) = 2m_q P^a(x), \quad (6)$$

where  $P^a(x) = \bar{\psi} \gamma_5 \frac{\tau^a}{2} \psi$  is the pseudoscalar density and  $m_q$  is the average quark mass in the isospin limit. The matrix element of the pseudoscalar density between single-nucleon states is given by

$$m_q \langle N(p', s') | P^a(0) | N(p, s) \rangle = m_q F_P(Q^2) (\bar{u}(p') \gamma_5 \frac{\tau^a}{2} u(p)), \quad (7)$$

where  $F_P(Q^2)$  is the pseudoscalar form factor. It is related to the pion-nucleon form factor  $G_{\pi N}(Q^2)$  through the relation [9]

$$m_q F_P(Q^2) = \frac{m_\pi^2 F_\pi}{m_\pi^2 + Q^2} G_{\pi N}(Q^2), \quad (8)$$

$F_\pi = 92.4 \text{ MeV}$  being the pion decay constant. Taking the matrix element of the PCAC relation in Eq. (6) between single-nucleon states provides another relation between the form factors in Eqs. (1) and (7),

$$2M_N G_A(Q^2) - \frac{Q^2}{2M_N} G_P(Q^2) = 2m_q F_P(Q^2). \quad (9)$$

In this work, we use this relation to study the form factors in Eq. (1). The induced pseudoscalar form factor has a pole at the pion mass, as dictated by chiral symmetry breaking via the Goldberger-Treiman [41–43] relation  $G_{\pi N}(Q^2) F_\pi = G_A(Q^2) M_N$  for  $Q^2 \rightarrow 0$ .

## B. Simulation details

The eleven ensembles used in this work are identical to those used in our calculation of electromagnetic form factors [44], and the reader is referred to Table I of Ref. [44] for details<sup>1</sup>. There are three lattice spacings,  $a = 0.079, 0.063$  and  $0.050 \text{ fm}$ , the lightest pion mass is  $190 \text{ MeV}$  and the physical volumes satisfy  $m_\pi L \geq 4.0$ . The ensembles, which were generated as part of the CLS (Coordinated Lattice Simulations) initiative, employ  $N_f = 2$  flavours of non-perturbatively  $\mathcal{O}(a)$ -improved Wilson fermions. The Monte Carlo simulations were performed using the deflation-accelerated DD-HMC [45, 46] and MP-HMC [47] algorithms. The value of the improvement coefficient  $c_{\text{sw}}$  was determined non-perturbatively in Ref. [48].

The setup for our lattice determination of the nucleon matrix element of the iso-vector axial current and pseudoscalar density is likewise very similar to the one we used in the case of the electromagnetic current [44]. We will always be

---

<sup>1</sup> Note that the number of measurements is identical to Ref. [44].

evaluating the third isospin component of the axial current and pseudoscalar density on the proton, and therefore drop isospin indices from now on. The nucleon two-point function is computed as

$$C_2(\mathbf{p}, t) = \sum_{\mathbf{x}} e^{i\mathbf{p}\cdot\mathbf{x}} \Gamma_{\beta\alpha} \langle \Psi^\alpha(\mathbf{x}, t) \bar{\Psi}^\beta(0) \rangle, \quad (10)$$

where  $\Psi^\alpha(\mathbf{x}, t)$  denotes the nucleon interpolating operator constructed as

$$\Psi^\alpha(x) = \epsilon_{abc} (\tilde{u}_a^T(x) C \gamma_5 \tilde{d}_b(x)) \tilde{u}_c^\alpha(x) \quad (11)$$

using Gaussian-smearred quark fields [49]

$$\tilde{\psi} = (1 + \kappa_G \Delta)^N \psi. \quad (12)$$

In Eq. (12), the gauge links entering the covariant three-dimensional Laplacian  $\Delta$  have been spatially APE-smearred [50] in order to reduce the gauge noise and to further enhance the projection properties onto the nucleon ground state. Our parameter choices for  $\kappa_G$  and  $N$  correspond to a smearing radius [51] of around  $r_{\text{sm}} \approx 0.5$  fm.

The nucleon three-point function is computed with the kinematics chosen such that the nucleon at the sink is always at rest, i.e.  $\mathbf{p}' = 0$ . This “fixed-sink” method allows for arbitrary insertion times for the current operator. In this work we consider the three-point functions with the local operator  $\mathcal{O}(\mathbf{y}, t) \in \{A_\mu^I, P\}$ , schematically represented as

$$C_{3,\mathcal{O}}(\mathbf{q}, t, t_s) = \sum_{\mathbf{x}, \mathbf{y}} e^{i\mathbf{q}\cdot\mathbf{y}} \Gamma_{\beta\alpha} \langle \Psi^\alpha(\mathbf{x}, t_s) \mathcal{O}(\mathbf{y}, t) \bar{\Psi}^\beta(0) \rangle, \quad (13)$$

where  $t_s$  denotes the nucleon source-sink separation, and  $t$  denotes the timeslice of the local operator insertion.

To ensure that all of our observables are  $\mathcal{O}(a)$ -improved, we use the renormalised iso-vector axial current including  $\mathcal{O}(a)$  improvement,

$$A_\mu^I(x) = Z_A (1 + b_A a m_q) (A_\mu(x) + a c_A \partial_\mu P(x)) \quad (14)$$

where  $A_\mu$  and  $P$  are the bare local axial current and pseudoscalar density, respectively, and  $m_q$  is the bare subtracted quark mass. The renormalisation factor  $Z_A$  and the improvement coefficient  $c_A$  have been determined non-perturbatively in Refs. [52] and [53], respectively, and the mass-dependent improvement coefficient  $b_A$  was computed in tadpole-improved perturbation theory in Ref. [54]. The pseudoscalar density is automatically  $\mathcal{O}(a)$  improved.

The projection matrix  $\Gamma$  is chosen as

$$\Gamma = \frac{1}{2} (1 + \gamma_0) (1 + i\gamma_5 \gamma_3) \quad (15)$$

and is identical to the one used in Ref. [44]. Both three-point and two-point functions are constructed using identical smearing at source and sink in order to ensure a positive spectral representation.

The matrix elements of the local operator  $\mathcal{O}(\mathbf{y}, t)$  are encoded in the three-point function and can be isolated by constructing appropriate ratios of the three-point and two-point functions, in which the normalisation of the interpolating operators cancels. We use the ratio

$$R_{\mathcal{O}}(\mathbf{q}, t, t_s) \equiv \frac{C_{3,\mathcal{O}}(\mathbf{q}, t, t_s)}{C_2(\mathbf{0}, t_s)} \sqrt{\frac{C_2(\mathbf{q}, t_s - t) C_2(\mathbf{0}, t) C_2(\mathbf{0}, t_s)}{C_2(\mathbf{0}, t_s - t) C_2(\mathbf{q}, t) C_2(\mathbf{q}, t_s)}}, \quad (16)$$

which was found to be particularly effective in isolating the ground-state matrix elements [55] in the asymptotic limit  $t, t_s \rightarrow \infty$ , where the single-nucleon state dominates.

### III. ANALYSIS OF EXCITED STATE CONTAMINATION

For the iso-vector axial current  $A_\mu^I(x)$  of Eq. (14) and using the projection matrix of Eq. (15), the asymptotic values  $R_{A_\mu}^0(\mathbf{q})$  of the ratios can be shown to have the following form:

$$\begin{aligned} R_{A_0}(\mathbf{q}, t, t_s) &\xrightarrow[t, t_s \rightarrow \infty]{} R_{A_0}^0(\mathbf{q}) \\ &= \frac{q_3}{\sqrt{2E_q(M_N + E_q)}} \left( G_A(Q^2) + \frac{M_N - E_q}{2M_N} G_P(Q^2) \right), \\ R_{A_k}(\mathbf{q}, t, t_s) &\xrightarrow[t, t_s \rightarrow \infty]{} R_{A_k}^0(\mathbf{q}) \\ &= \frac{i}{\sqrt{2E_q(M_N + E_q)}} \left( (M_N + E_q) G_A(Q^2) \delta_{3k} - \frac{G_P(Q^2)}{2M_N} q_3 q_k \right), \end{aligned} \quad (17)$$

where  $E_q$  is the energy of a nucleon with momentum  $\mathbf{q}$  as given by the lattice dispersion relation.

The ratio of the pseudoscalar density  $R_P^0(\mathbf{q})$  also provides access to the axial and induced pseudoscalar form factors via the PCAC relation in Eqs. (6) and (9), with an asymptotic value given by

$$2m_q R_P(\mathbf{q}, t, t_s) \xrightarrow[t, t_s \rightarrow \infty]{} 2m_q R_P^0(\mathbf{q}) = 2M_N R_{A_0}^0(\mathbf{q}) \quad (18)$$

We note that the PCAC relation implies that the product of the bare quark mass and the pseudoscalar density is renormalised by the renormalisation constant  $Z_A$  of the axial current. However, in the course of our analysis we found that the temporal component  $A_0$  of the axial current was too noisy and too affected by excited-state contributions to be included in the determination of the form factors.

In the asymptotic ratios  $R_{A,P}^0$  of the axial current and pseudoscalar density, the axial and induced pseudoscalar form factors  $G_{A,P}$  appear in linear combinations, from which they can be determined by solving the (generally overdetermined) linear system in Eq. (17). For a given four-momentum transfer  $Q^2$ , this is done by minimizing the least-squares function

$$\chi^2 = \sum_{i,j}^N (\mathbf{R} - \mathbf{M} \mathbf{G})_i (\sigma^{-2})_{ij} (\mathbf{R} - \mathbf{M} \mathbf{G})_j, \quad (19)$$

where  $\sigma^2$  is the covariance matrix of the ratios  $R_i$  and

$$\mathbf{R} = \begin{pmatrix} R_1 \\ \vdots \\ R_N \end{pmatrix}, \quad \mathbf{M} = \begin{pmatrix} M_{1,A} & M_{1,P} \\ \vdots & \vdots \\ M_{N,A} & M_{N,P} \end{pmatrix}, \quad \mathbf{G} = \begin{pmatrix} G_A \\ G_P \end{pmatrix}.$$

At each four-momentum transfer  $Q^2$ , the ratios for those individual three-momentum vectors  $\mathbf{q}$  which are related by an exact symmetry of the lattice are averaged, and the resulting averaged ratios are combined into the vector  $\mathbf{R}^\top = (R_1 \dots R_N)$ . In Table I, we list, for each momentum transfer, the number  $N$  of ratios coming from the various components of the axial current and the pseudoscalar density which remain after averaging over equivalent momenta. The kinematic factors associated with each of the averaged ratios are represented by the rectangular matrix  $\mathbf{M}$  of size  $(N \times 2)$ .

In obtaining the form factors from the measured ratios, we can proceed in two different ways, which differ by the order in which the extraction of the asymptotic behaviour and the reduction into form factors are performed:

1. *Computing effective form factors:* In this approach, the linear system resulting from Eq. (19) is solved for each operator insertion time  $t$ , source-sink separation  $t_s$ , and four-momentum transfer  $Q^2$ , yielding the so-called effective form factors  $G_{A,P}^{\text{eff}}(Q^2, t, t_s)$ . The effective form factors still contain short-distance contributions from multi-particle and excited states, which need to be accounted for in order to determine the ground-state form factors; we will discuss the methods used for this purpose below. This method allows for the visualisation of the approach of  $G_{A,P}^{\text{eff}}(Q^2, t, t_s)$  towards the ground-state form factors  $G_{A,P}(Q^2)$  as  $t, t_s \rightarrow \infty$  (cf. Fig. 4).
2. *Computing asymptotic ratios:* In this approach, the excited-state analysis is first applied to the vector of averaged ratios  $\mathbf{R}(Q^2, t, t_s)$  in order to obtain asymptotic ratios  $\mathbf{R}^0(Q^2)$  for  $t, t_s \rightarrow \infty$ . The linear system resulting from (19) is then solved on these asymptotic ratios, which then directly yields the ground-state form factors  $G_{A,P}(Q^2)$ .

TABLE I. Numbers of momentum-averaged components of the axial current  $A_\mu(x)$  and pseudoscalar density  $P(x)$  available for solving the linear system in Eq. (19) at various momentum transfers.

$\frac{q^2 L^2}{4\pi^2}$	$A_{1,2}$	$A_3$	$P$	$N$
0	-	1	-	1
1	0	2	1	3
2	1	2	1	4
3	1	1	1	3
4	0	2	1	3
5	1	3	2	6
6	2	2	2	6

The determination of the asymptotic quantities from their effective counterparts is rendered non-trivial by the combination of the exponentially decaying signal-to-noise ratio of baryonic correlation functions at large time separations and the presence at short time separations of contributions from excited and multi-particle states. These excited-state contributions vanish exponentially and give rise to corrections of the form

$$G_{A,P}^{\text{eff}}(Q^2, t, t_s) = G_{A,P}(Q^2) \times \left( 1 + \mathcal{O}(e^{-\Delta t}) + \mathcal{O}(e^{-\Delta'(t_s-t)}) \right), \quad (20)$$

where  $\Delta$  and  $\Delta'$  are the energy gaps between the ground and excited states of the initial and final-state nucleons. A corresponding relation holds between the ratios  $\mathbf{R}(Q^2, t, t_s)$  and their asymptotic values  $\mathbf{R}^0(Q^2)$ . While the contributions from excited states can in principle be made exponentially small by taking both  $t$  and  $t_s - t$  to be large, the exponential decrease of the signal-to-noise ratio makes this approach impracticable, as very high statistics would be required to go significantly beyond  $t_s \sim 1.2$  fm.<sup>2</sup> As previously observed [44], a source-sink separation of at least  $t_s \gtrsim 0.5$  fm is required to achieve ground-state saturation in the two-point function for single nucleon states with zero momentum. For nucleon states with non-zero momenta the limitation is even more severe, and in the case of three-point functions, both  $t$  and  $t_s - t$  must be made sufficiently large, so that source-sink separations larger than  $t_s > 1.5$  fm would be required to achieve ground-state saturation. At the currently achievable source-sink separations of  $t_s \sim 1 - 1.2$  fm used in this work, we can therefore not rely on ground-state saturation, and a systematic analysis of the excited state contributions is necessary. In our previous work [18, 44, 58, 59], we have found two methods to be particularly useful in studying the excited-state contributions, namely

- A. *Summation method:* This method starts from constructing summed ratios [17, 60–62] at each four-momentum transfer  $Q^2$  and source-sink separation  $t_s$ . The summed ratios can be shown to be asymptotically linear in the source-sink separation  $t_s$ , with the form factors  $G_{A,P}$  appearing as the slope,

$$S(t_s) \equiv \sum_{t=1}^{t_s-1} G_{A,P}^{\text{eff}}(Q^2, t, t_s) \rightarrow K(Q^2) + t_s G_{A,P}(Q^2) + \dots, \quad (21)$$

where  $K(Q^2)$  denotes a constant intercept, and the ellipses indicate neglected subleading contributions of  $\mathcal{O}(t_s e^{-\Delta t_s})$  and  $\mathcal{O}(t_s e^{-\Delta' t_s})$ .

<sup>2</sup> However, the use of techniques such as all-mode-averaging [56, 57] may provide a means to study source-sink separations as large as  $t_s \sim 1.6$  fm with reasonable statistical accuracy [30].

B. *Two-state fits*: In this method, the excited-state contributions are explicitly modelled using the ansatz

$$G_{A,P}^{\text{eff}}(Q^2, t, t_s) = G_{A,P}(Q^2) + c_1(Q^2) e^{-\Delta t} + c_2(Q^2) e^{-\Delta'(t_s-t)}, \quad (22)$$

where the ground-state form factors  $G_{A,P}(Q^2)$  and amplitudes  $c_1(Q^2)$ ,  $c_2(Q^2)$  are determined by fitting Eq. (22) to the data for all source-sink separations  $t_s$  and insertion times  $t$  at each value of the four-momentum transfer  $Q^2$ . In the case of the axial charge, we are also able to determine the amplitude of the transition from the excited state to the excited state, due to the symmetry of the three-point function under the transformation  $t \rightarrow (t_s - t)$  – see Eq. (24) below. We have used the ansatz (22) to perform two-state fits in our previous study of nucleon electromagnetic form factors [44]. We note that in Refs. [37, 38] the term “two-state fit” denotes an ansatz that also includes the excited-to-excited contribution. In principle, the gaps  $\Delta$ ,  $\Delta'$  can be determined from the fits; in practice, however, we have found the resulting fits to be unstable, and in order to obtain meaningful uncertainties in the fit parameters, an explicit ansatz is made for the gaps. On our lattice ensembles, we expect the low-lying energy levels to be separated typically by several hundred MeV. With our source-sink separations  $t_s \gtrsim 1$  fm, the higher excited states should then be suppressed in the three-point correlation function. The simplest model for the excited nucleon spectrum consists of a set of non-interacting multi-hadron states. In our setup, the initial-state nucleon is moving, which motivates the ansatz of an  $N\pi$  state with the pion at rest for the dominant excited-state contribution, corresponding to a gap  $\Delta = m_\pi$ . The final-state nucleon, on the other hand, is at rest, motivating the ansatz of an  $S$ -wave  $N\pi\pi$  state with gap  $\Delta' = 2m_\pi$  for the dominant excited-state contribution. In Ref. [63], the  $N\pi$  excited spectrum was investigated thoroughly at physical quark masses, including the effects of interactions via the experimentally known  $P$ -wave scattering phase. The effect of the interaction on the energy level is small, and at the volumes of  $m_\pi L \approx 4$  investigated here, the first excited  $N\pi$  state is practically degenerate with the  $S$ -wave  $N\pi\pi$  state when interactions are neglected.

Setting the finite-volume energy gaps to the values corresponding to no interactions between pions and the nucleon may introduce a systematic bias in the two-state fit method. The summation method, on the other hand, makes no specific assumptions about the values of the energy gaps; it only assumes that terms of order  $e^{-\Delta^{(\prime)}t_s}$  can be neglected.

The summation method thus involves weaker assumptions about the excited-state contamination than our implementation of the two-state fit method. On the other hand, both methods neglect terms of order  $e^{-\Delta^{(\prime)}t_s}$  in the spectral representation. Therefore, in order to assess the stability of the physics results under variations of the analysis procedure, we apply both methods in our study of the axial and induced pseudoscalar form factors  $G_{A,P}(Q^2)$  of the nucleon.

## IV. ISOVECTOR AXIAL FORM FACTOR

### A. Axial charge

The axial charge  $g_A = G_A(0)$  can be determined directly from the matrix element of the  $z$ -component of the axial current  $A_3$  at zero momentum transfer where the ratio in Eq. (16) takes the simplified form

$$g_A^{\text{eff}}(t, t_s) \equiv R_{A_3}(0, t, t_s) = \frac{C_{A_3}(0, t, t_s)}{C_2(0, t_s)}. \quad (23)$$

Since the initial and the final states are identical, the excited state contributions will be the same at source and sink, and we expect the effective axial charge  $g_A^{\text{eff}}(t, t_s)$  to approach its asymptotic value in a symmetric fashion. Moreover, since the nucleon is at rest in the initial and final state, we expect the dominant excited-state contributions can arise from the  $S$ -wave  $N\pi\pi$  multiparticle state, i.e. a nucleon and two pions at rest, leading to the ansatz  $\Delta = \Delta' = 2m_\pi$  for the mass gap. For analytic studies of the excited-state contamination based on chiral effective theory, see [64–66], and [63] for a study based on Lüscher’s finite-volume formalism. In the two-state fits for the axial charge, we therefore use the fit form

$$g_A^{\text{eff}}(t, t_s) = g_A + \tilde{c}_1 \left( e^{-2m_\pi t} + e^{-2m_\pi(t_s-t)} \right) + \tilde{c}_2 e^{-2m_\pi t_s}, \quad (24)$$

where  $m_\pi$  is fixed to the pion mass on the ensemble.

In the left panel of Fig. 1, results for the axial charge on the N6 ensemble are shown, where the effective axial charge is computed for four source-sink separations ranging from  $t_s = 0.6$  fm to  $t_s = 1.1$  fm. The symmetric approach

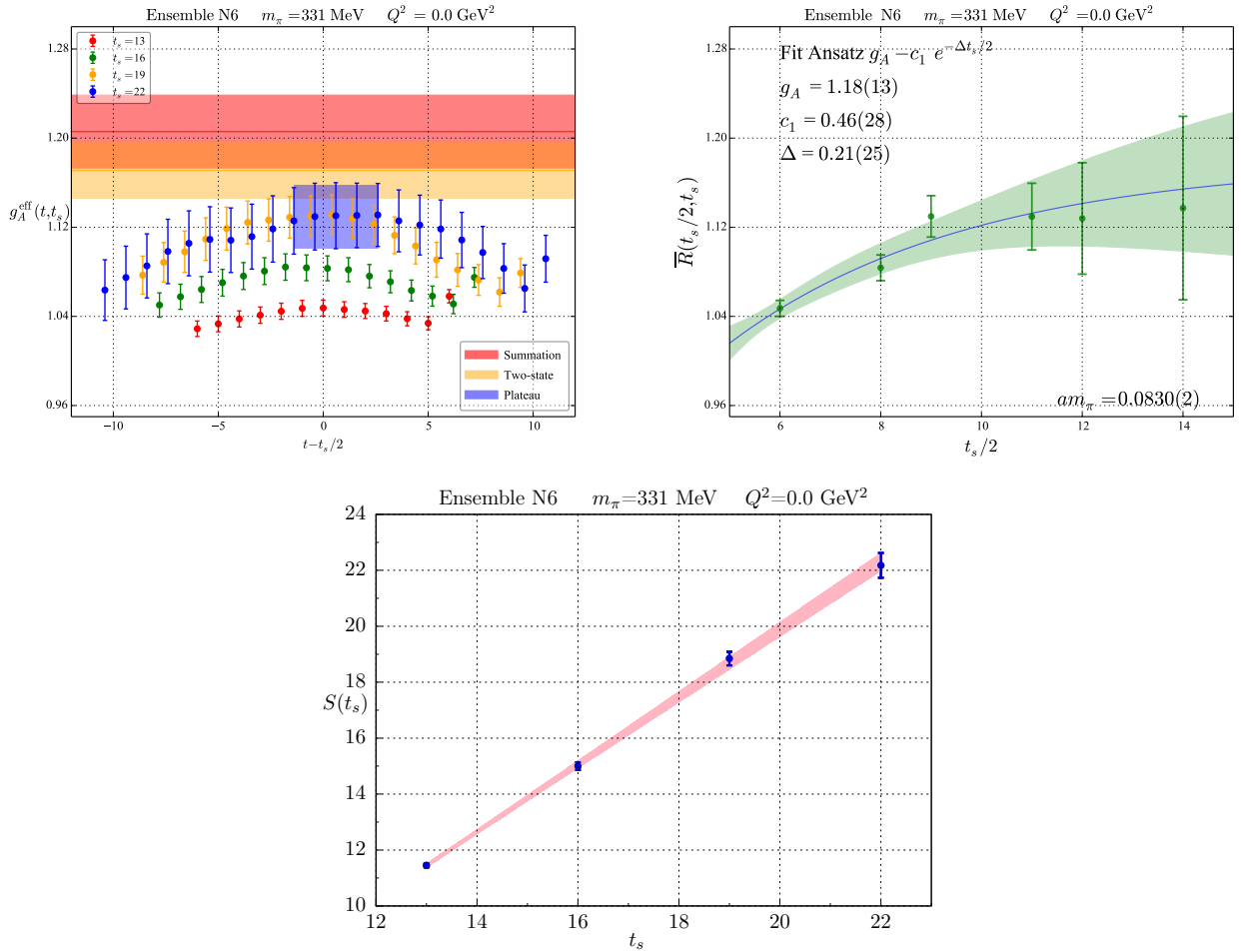


FIG. 1. Left panel: Effective axial charge  $g_A^{\text{eff}}(t, t_s)$  on Ensemble N6; different source-sink separations  $t_s$  are displayed in different colours; also shown are a plateau fit (blue band) at the largest source-sink separation  $t_s = 22a \approx 1.1$  fm, and the results for  $g_A$  obtained using the summation method (red band) and a two-state fit (yellow band). Right Panel: Results of plateau fits at different source-sink separations  $t_s$  with a fit to the expected  $t_s$ -dependence. Bottom panel: illustration of the summation method, where  $S(\tau = t_s)$  is the summed insertion (21). The slope corresponds to the axial charge.

to the central plateau region can clearly be seen. The data also exhibit a discrepancy between the midpoint values  $g_A^{\text{eff}}(t_s/2, t_s)$  reached at different source-sink separations, indicating that excited-state contaminations are still present even when the ratio has apparently reached a plateau. To investigate the excited-state contribution in the plateau region further, the dataset was expanded to include source-sink separations of  $t_s = 1.3$  fm and  $t_s = 1.4$  fm. The right panel of Fig. 1 shows the results from applying a plateau fit to the data at  $t = t_s/2 \pm 2^3$  for different source-sink separations  $t_s$ . The dependence of the fit results on  $t_s$  can be seen clearly. While the large errors at the largest source-sink separations  $t_s > 1.1$  fm somewhat obscure the trend, it is clear that  $g_A$  may be underestimated when using plateau fits, and we do not employ plateau fits in our further analysis. Also shown is a fit to the expected  $t_s$ -dependence, taking the energy gap to the excited state as a free parameter. The fit results are compatible with the assumption of a dominant S-wave  $N\pi\pi$  state, although the uncertainty on the fit parameters is too large to make a conclusive argument.

The results of various fit procedures are shown as coloured bands in the left panel of Fig. 1. The blue band indicates a plateau fit to source-sink separation  $t = 1.1$  fm, which is seen to lie significantly below the results of both of the analysis methods used in the following: the yellow band is a simultaneous fit to all source-sink separations  $t_s$  and operator insertion times  $t$  up to 1.1 fm to the ansatz of Eq. (24), and the red band indicates the result obtained using

<sup>3</sup> For source-sink separations that are odd in lattice units, plateaus are fitted at  $(t_s - 1)/2 \pm 2$



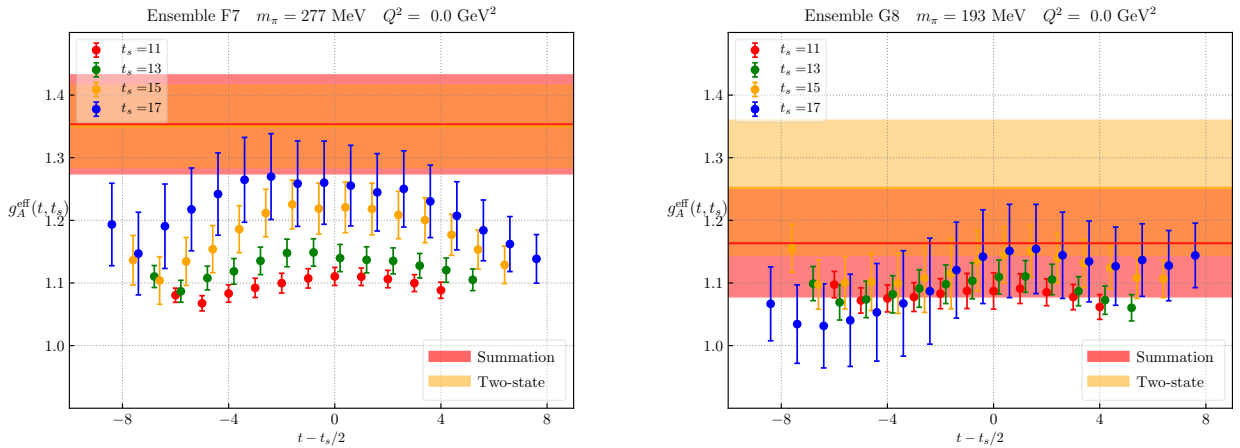


FIG. 2. The effective axial charge on the ensembles F7 ( $m_\pi = 277$  MeV, left panel) and G8 ( $m_\pi = 193$  MeV, right panel). Different source-sink separations  $t_s$  are displayed in different colours; the bands represent the result for the axial charge obtained using the summation method (red band) and a two-state fit (yellow band) to extract ground-state matrix elements.

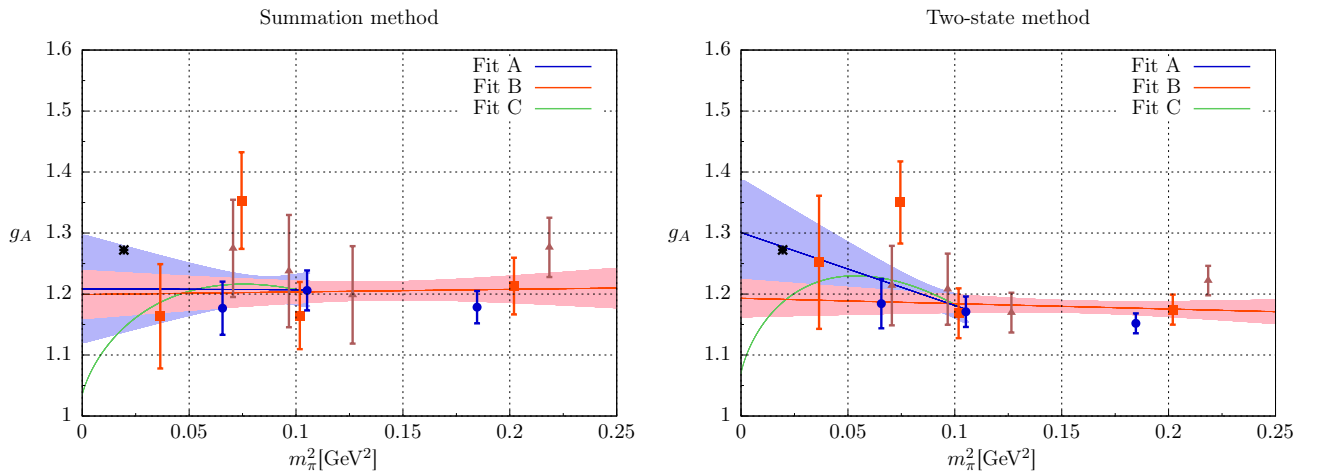


FIG. 3. Chiral extrapolation of the axial charge  $g_A$  obtained using the summation method (left panel) and a two-state fit (right panel) to the physical pion mass. Triangles, squares and circles correspond to increasingly fine lattice spacings, and the black point represents the phenomenological value of  $g_A$ . Fit A is a linear fit with a pion-mass cut  $m_\pi \leq 335$  MeV, Fit B is a linear fit with no pion-mass cut, and Fit C is based on chiral effective theory via the ansatz of Eq. (32).

the summation method. The quality of the linear fit performed in the latter method is illustrated in the bottom panel of Fig. 1. The results from the two-state fit and summation method agree very well with each other, indicating that residual excited-state effects are likely small on this ensemble. The effective axial charge on two of our most chiral ensembles is displayed in Fig. 2, together with the results of the summation and excited-state fits shown as bands. On ensemble F7, the two analysis methods are in very close agreement, while on G8 they differ in their result for  $g_A$  by one standard deviation.

In Fig. 3, the results for  $g_A$  obtained using the summation method (left panel) and two-state fits (right panel) on each of our ensembles are shown together with a chiral extrapolation to the physical pion mass. Details of the chiral extrapolation procedure will be presented in section VI. Here we note that the ensembles employed in our work all obey the constraint  $m_\pi L \geq 4$ , and hence finite-volume effects are expected to be small. This is also supported empirically by our data, which do not display any noticeable volume dependence of  $g_A$ . Similarly, no discernable dependence of  $g_A$  on the lattice spacing is found in Fig. 3 for  $m_\pi \leq 335$  MeV.

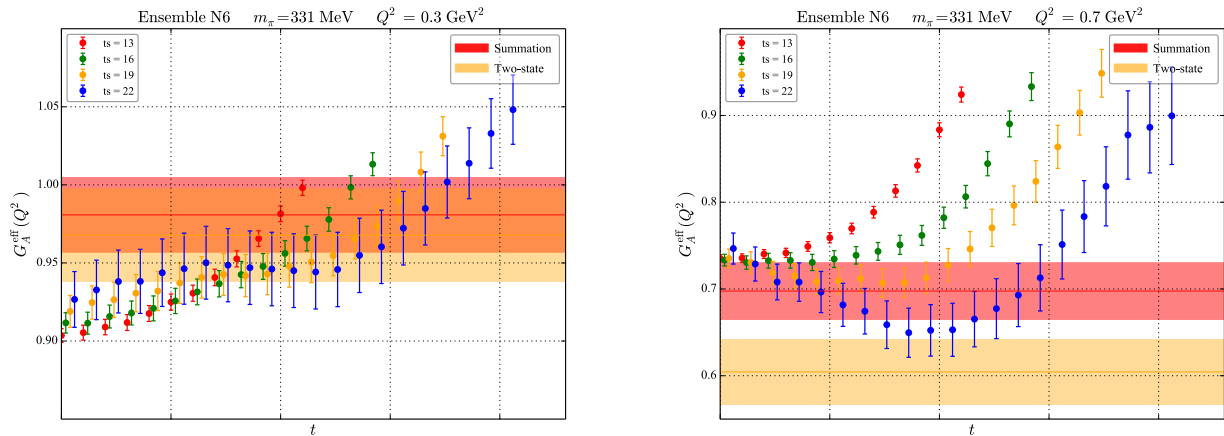


FIG. 4. The effective axial form factor  $G_A^{\text{eff}}$  on the N6 ensemble at four-momentum transfers of  $Q^2 = 0.3 \text{ GeV}^2$  (left panel; corresponding to  $(\frac{L\mathbf{q}}{2\pi})^2 = 1$ ) and  $Q^2 = 0.7 \text{ GeV}^2$  (right panel; corresponding to  $(\frac{L\mathbf{q}}{2\pi})^2 = 3$ ). The bands represent the result for  $G_A(Q^2)$  obtained using the summation and the two-state-fit methods to extract asymptotic ratios, after which the linear system resulting from Eq. (19) is solved for  $(G_A, G_P)$ .

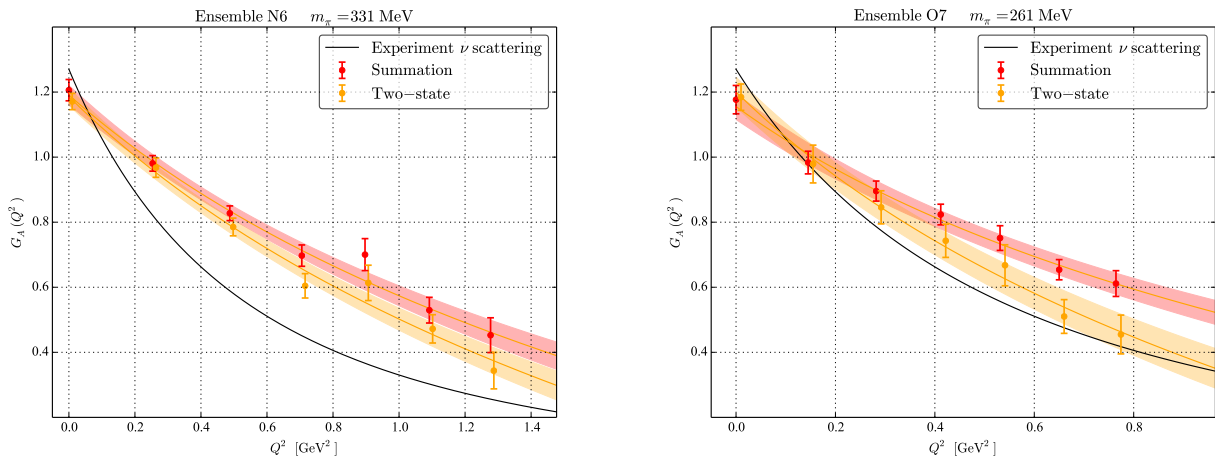


FIG. 5. Momentum-transfer dependence of the axial form factor  $G_A(Q^2)$  on the ensembles N6 (left panel) and O7 (right panel). The solid black line shows a dipole parameterisation of experimental data [8].

## B. Momentum-transfer dependence of the axial form factor

At non-zero momentum transfer, the determination of the axial form factor becomes more involved. In our choice of reference frame, the  $t$  dependence of the effective form factors is no longer symmetric about the point  $t = t_s/2$ ; as a consequence, we apply Eq. (22), as opposed to Eq. (24), when using the two-state fit method. Furthermore, both  $G_A$  and  $G_P$  contribute to the matrix elements and must be separated by solving the linear system of Eq. (19). As described above in section III, there are two ways in which the solution of the linear system can be combined with the analysis methods to account for excited-state contributions in order to extract the ground-state form factors, and we shall employ both of these in the following. Moreover, through the PCAC relation the matrix element of the pseudoscalar density provides an additional observable that can be used in conjunction with the matrix elements of the components of the axial current in order to determine the axial-current form factors. In the case of the axial form factor, we find that the determination of the form factor  $G_A$  is relatively stable against the inclusion and exclusion of the pseudoscalar density in our basis of operators.

The results of evaluating the effective axial form factor  $G_A^{\text{eff}}(Q^2, t, t_s)$  on the N6 ensemble at the four-momentum transfers of  $Q^2 = 0.3 \text{ GeV}^2$  and  $Q^2 = 0.7 \text{ GeV}^2$  are shown in Fig. 4. At  $Q^2 = 0.3 \text{ GeV}^2$ , which is the lowest non-

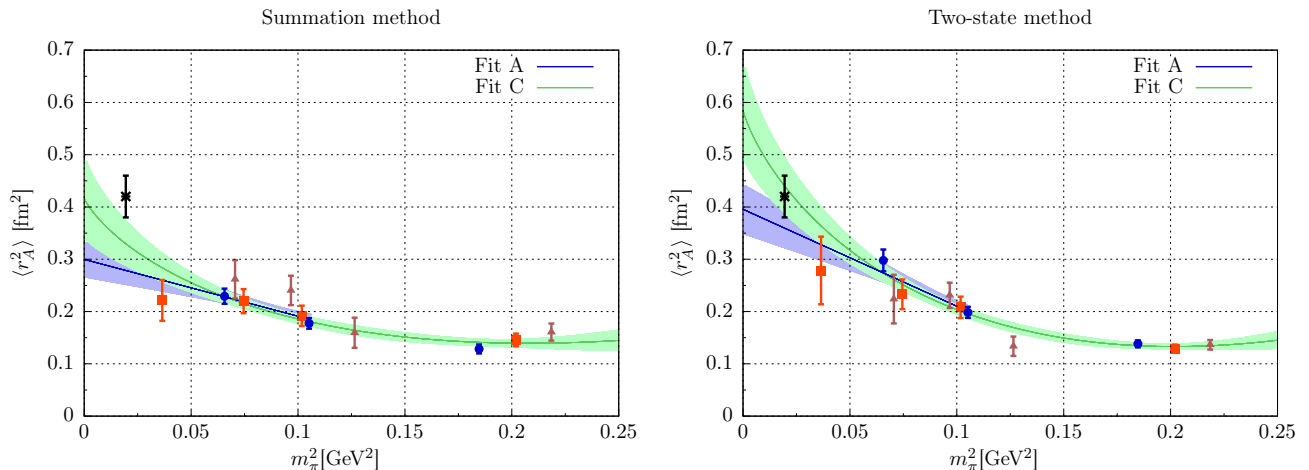


FIG. 6. Results for the squared axial radius  $\langle r_A^2 \rangle$  from the  $z$ -expansion applied to the summation method (left panel) and two-state fit (right panel) results for  $G_A(Q^2)$ . Triangles, squares and circles correspond to increasingly fine lattice spacings, and the black point represents the phenomenological value of  $\langle r_A^2 \rangle$  [67]. Fit A is a linear fit (30) with a pion-mass cut  $m_\pi \leq 335$  MeV, and Fit C is based on the ansatz (31) with no pion-mass cut.

TABLE II. Results for  $\chi^2/\text{dof}$  of the linear system in Eq. (19) for each of the analysis methods used on Ensemble N6 when including or excluding the pseudoscalar density  $P(x)$ .

	Summation Method		Two-state Method	
	$\chi^2/\text{dof}$ with $P(x)$	$\chi^2/\text{dof}$ without $P(x)$	$\chi^2/\text{dof}$ with $P(x)$	$\chi^2/\text{dof}$ without $P(x)$
1	90.0	n/a	1.85	n/a
2	23.3	0.41	0.13	0.26
3	19.8	n/a	0.07	n/a
4	15.2	n/a	1.88	n/a
5	3.09	1.59	1.03	0.21
6	1.76	0.23	1.10	0.02

vanishing four-momentum transfer that can be realised on this ensemble, no clear plateau appears for source-sink separations in the range of  $t_s = 0.6 - 1.0$  fm, and for the largest source-sink separation  $t_s = 1.1$  fm, the size of the uncertainties on the data make it difficult to decide whether a plateau has truly been reached.

Also shown are bands indicating the results of fitting the effective form factor using a two-state fit (Eq. (22)) and the summation method (Eq. (21)), and it can be seen that these agree with each other within their respective uncertainties. At the larger four-momentum transfer of  $Q^2 = 0.7$  GeV<sup>2</sup>, on the other hand, the results for the effective form factor  $G_A^{\text{eff}}(Q^2, t, t_s)$  at different source-sink separations  $t_s$  show a clear downward trend in the central region,  $t \approx t_s/2$ , where excited state contributions are expected to be most strongly suppressed, indicating that the plateau has not stabilized for  $t_s \gtrsim 1.1$  fm. Furthermore, the results for  $G_A(Q^2)$  obtained using the summation method and two-state fits are not in agreement with each other, which may be due to the more statistically precise data at the lower source-sink separations having a disproportionately strong influence on the fit results. This may introduce a bias in the two-state fit, but is likely to affect the slope of the summed ratio in the summation method even more. We will return to considering the relative reliability of the two methods when discussing the induced pseudoscalar form factor.

To confirm the stability of our analysis, we have verified that we obtain the same results for the axial form factor  $G_A(Q^2)$  at each four-momentum transfer  $Q^2$  when we fit to the asymptotic behaviour of the effective form factors, and when we first extract the asymptotic behaviour of the ratios before isolating the form factors (i.e. methods 1 and 2 of section III yield consistent results). The values of  $\chi^2/\text{dof}$  obtained when solving the linear system of Eq. (19) after extracting asymptotic ratios using the summation method or two-state fits are shown in Table II. The values of  $\chi^2/\text{dof}$  obtained with the summation method are large when  $P(x)$  is included. Nevertheless the results for the axial form factor are quite stable, regardless of whether the pseudoscalar density  $P(x)$  is excluded or included in the analysis. This may be attributed largely to the fact that the inclusion of  $P(x)$  affects the results for the induced pseudoscalar form factor  $G_P(Q^2)$  much more strongly than those for  $G_A(Q^2)$ ; we will further remark on this when discussing the induced pseudoscalar form factor in section V. When extracting the asymptotic ratios using two-state fits, the values of  $\chi^2/\text{dof}$  for Eq. (19) are rather reasonable both when including and when excluding the pseudoscalar density, and the results for  $G_A(Q^2)$  (and for  $G_P(Q^2)$ , as discussed in section V) are likewise compatible.

The momentum-transfer dependence of the axial form factor is shown in Fig. 5 for the ensembles N6 ( $m_\pi = 331$  MeV) and O7 ( $m_\pi = 261$  MeV). We note that while the results from the summation method and from two-state fits agree well near  $Q^2 = 0$ , the disagreement between them becomes larger with increasing  $Q^2$ , where the two-state fits tend to approach more closely the shape of the form factor inferred from experimental results, and this trend becomes more pronounced as the pion mass is decreased towards the physical point. We also note that (as previously observed elsewhere [16–22, 24–28]) while the lattice calculations tend to underestimate the axial charge, they tend to overestimate the value of the form factor at non-vanishing four-momentum transfer, leading to an underestimation of the axial radius of the nucleon.

### C. Model-independent determination of $\langle r_A^2 \rangle$

While the momentum-transfer dependence of the axial form factor is frequently modelled with a dipole fit [8], this leads to a model-dependence of the determination of the axial charge radius  $\langle r_A^2 \rangle^{1/2}$ . Moreover, the use of the momentum transfer  $Q^2$  as the expansion variable has been shown to have a small radius of convergence, and the use of a conformally mapped parameter  $z(Q^2)$  has been suggested [68, 69] in order to improve the convergence by parameterising the form factor in a model-independent manner as a power series in  $z(Q^2)$ . The definition of  $z(Q^2)$  and the corresponding power series for the form factor are given by

$$z(Q^2) = \frac{\sqrt{t_{\text{cut}} + Q^2} - \sqrt{t_{\text{cut}}}}{\sqrt{t_{\text{cut}} + Q^2} + \sqrt{t_{\text{cut}}}}, \quad G_A(Q^2) = \sum_{n=0}^{\infty} a_n z^n(Q^2), \quad (25)$$

where  $t_{\text{cut}} = 9m_\pi^2$  is the three-pion kinematic threshold in the iso-vector axial-current channel. The power-series expansion of the form factor shown in Eq. (25) provides a controlled way of obtaining observables such as the axial radius in a model-independent fashion: once the coefficients  $a_n$  have been determined from a fit to Eq. (25), the axial radius as defined in Eq. (4) can be derived from them in a straightforward manner.

In this work, we have studied up to  $n_{\text{max}} = 4$  orders in the  $z$ -expansion of Eq. (25), and the results at different orders were found to be consistent, provided that Bayesian priors were used to stabilize the fit; otherwise, the fits beyond  $n_{\text{max}} = 1$  became too unstable. While we have checked that the results for the axial charge radius obtained from the  $z$ -expansion were stable against variations of the priors, we quote only the results obtained using the first order of the  $z$ -expansion, where no priors were applied. The results obtained for the axial charge radius on our set of ensembles using the summation method and two-state fits are given in Tab. XVII and presented in Fig. 6 together with a chiral extrapolation to the physical pion mass. For details of the chiral extrapolation, the reader is referred to section VI. For now, we make the qualitative observation that the mean-square radius increases by roughly a factor two between  $m_\pi = 430$  MeV and  $m_\pi = 270$  MeV. Similar to the axial charge, no systematic trend of the axial radius as a function of the lattice spacing is seen.

## V. ISOVECTOR INDUCED PSEUDOSCALAR FORM FACTOR

The momentum transfer dependence of the induced pseudoscalar form factor  $G_P(Q^2)$  is markedly different from that of the axial form factor due to the presence of a pole at the pion mass arising as a consequence of chiral symmetry breaking. The low-momentum behaviour of  $G_P(Q^2)$  may therefore be expected to be rather steep, with possibly considerable statistical fluctuations in the low- $Q^2$  region. In this section, we discuss the determination of the induced pseudoscalar form factor from our various analysis methods for suppressing excited-state contributions, and how these are affected by the choice of either including or excluding the pseudoscalar density in our operator basis.

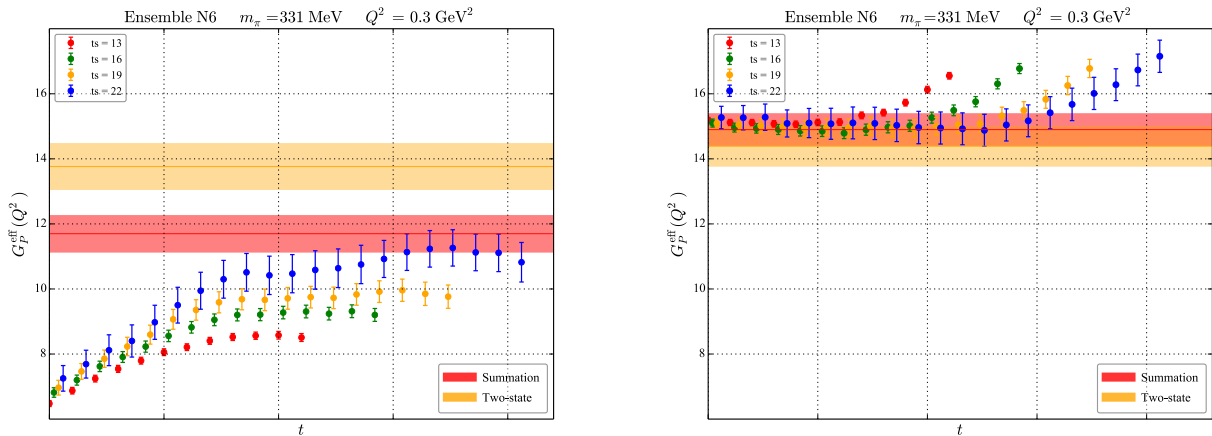


FIG. 7. Effective induced pseudoscalar form factor on the N6 ensemble at four-momentum transfer  $Q^2 = 0.3 \text{ GeV}^2$  when excluding (left panel) and including (right panel) the pseudoscalar density  $P(x)$  in the basis of ratios used to extract the form factors. The bands represent the result for  $G_P(Q^2)$  obtained using the summation and the two-state-fit methods to extract asymptotic ratios, after which the linear system resulting from Eq. (19) is solved for  $(G_A, G_P)$ .

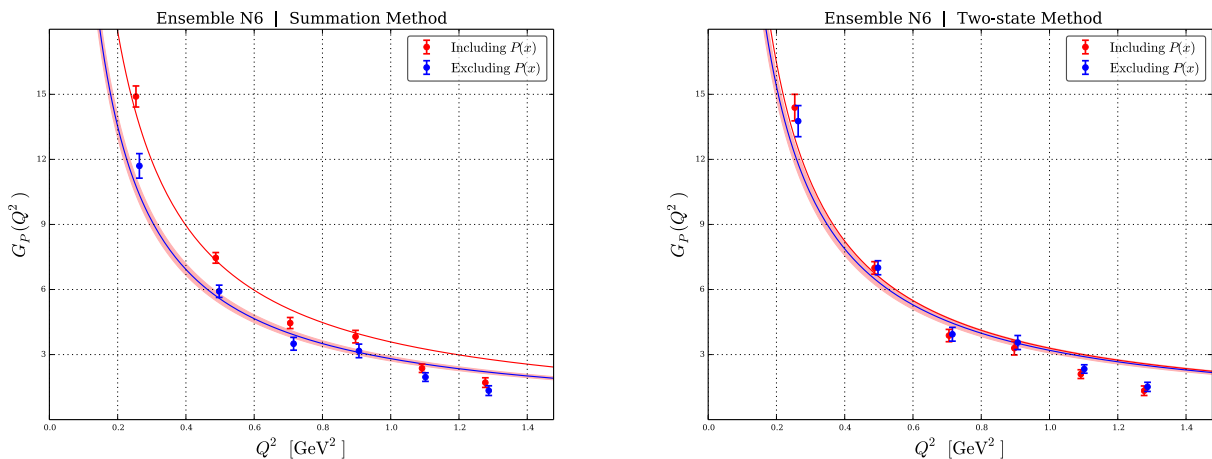


FIG. 8. Results for the induced pseudoscalar form factor obtained by solving Eq. (19) for the asymptotic ratios on the N6 ensemble using the summation method (left panel) and two-state fits (right panel). The curves represent a fit using the Goldberger-Treiman-inspired pion-pole parameterization  $G_P(Q^2) = 4M_N^2 G_A(Q^2)/(Q^2 + m_\pi^2)$ , where  $M_N$  and  $m_\pi$  are obtained from the fit.

Relation (9) expresses the PCAC relation at the level of ground-state matrix elements. Since the extraction of the latter from the three-point function comes with an additional uncertainty due to potential contamination from excited states, we initially test the PCAC relation at the correlator level,

$$\frac{R_{A_0}(\mathbf{q}, t, t_s)}{C_{3,A_0}(\mathbf{q}, t, t_s)} \frac{1}{2a} \left( C_{3,A_0}(\mathbf{q}, t+a, t_s) - C_{3,A_0}(\mathbf{q}, t-a, t_s) \right) - i \sum_{k=1}^3 q_k R_{A_k}(\mathbf{q}, t, t_s) - 2m_q R_P(\mathbf{q}, t, t_s) = O(a^2). \quad (26)$$

We have checked that the left-hand side has an average compatible with zero. For instance, on ensemble O7 at the smallest available spatial momentum, the absolute statistical uncertainty on the left-hand side is no more than 0.01 for all values of  $t$  and  $t_s$  [70]. Thus the violation of the PCAC relation due to discretization errors appears to be small. Therefore, we adopt the point of view that the consistency condition (9) on the ground-state matrix elements can be used as a way to test the ability of the summation method and the two-state fits to extract the ground-state matrix elements.

In order to gain insight into the nature of the excited-state contributions, we first construct the effective form factor  $G_P^{\text{eff}}(Q^2, t, t_s)$  by solving the linear system of Eq. (19) at each four-momentum  $Q^2$ , operator insertion time  $t$ , and source-sink separation  $t_s$ . In doing so, we find a marked difference in the time-separation dependence of  $G_P^{\text{eff}}(Q^2, t, t_s)$  between the case where only components of the axial current are included in solving Eq. (19) and the case where a combination of components of the axial current  $A_i(x)$  as well as pseudoscalar density  $P(x)$  are included. This is in contrast to the situation for the axial form factor  $G_A(Q^2)$ , where no strong dependence on the inclusion or exclusion of  $P(x)$  in the operator basis was observed. The results for both cases are shown in Fig. 7. It can be clearly seen that the choice of whether to include the pseudoscalar density  $P(x)$  has a significant and non-trivial impact on the time-dependence of the effective induced pseudoscalar form factor. For the case where only the axial current is included in the determination (shown in the left panel of Fig. 7), the results asymptote from below, with much stronger excited-state effects visible at the source as compared to the sink. The apparent plateaux reached at different source-sink separations  $t_s$  do not agree with each other, indicating that the contribution from excited states is substantial at time separations as large as 1.1 fm. For the case where both the pseudoscalar density and the axial current are included in the determination (shown in the right panel of Fig. 7), the results are much less time-dependent and asymptote from above, with stronger excited-state effects seen at the sink rather than the source. The plateaux for different source-sink separations  $t_s$  agree with each other within their respective statistical uncertainties. However, the plateau values differ significantly from those seen when excluding  $P(x)$ , even at the largest source-sink separations, which further indicates that excited-state contamination remains a significant effect even at  $t_s \sim 1.1$  fm.

Also shown in Fig. 7 are the results of applying each of our excited-state analysis methods, *viz.* the summation method (red bands) and two-state fits (yellow bands). It can be seen that when extracting the induced pseudoscalar form factor using only the axial current, the results from the two methods disagree significantly, which may indicate that excited-state effects are not under control. When including the pseudoscalar density in the determination, on the other hand, the results from the summation and two-state methods agree within their respective error bands. As pointed out in section IV, the matrix elements of the pseudoscalar density are found to be statistically more precise in comparison to those of the axial current, and hence strongly influence the determination of the effective form factors. Their impact on the results seems to be limited to the induced pseudoscalar form factor, however. Judging both from the appearance of the effective form factor and from the agreement between our analysis methods, the excited-state effects seem to be smaller in the case where the pseudoscalar density is included. We conclude that its inclusion is beneficial and therefore keep the pseudoscalar density as part of all subsequent analyses.

The dependence on  $Q^2$  of the results obtained using each of our analysis methods when including or excluding the pseudoscalar density  $P(x)$  in the solution of Eq. (19) is presented in Fig. 8. The form factors obtained with the summation method (shown in the left panel of Fig. 8) can be seen to be particularly sensitive to the inclusion of the pseudoscalar density, with a clear gap opening up particularly in the low- $Q^2$  regime. This is also evident from the large values of  $\chi^2/\text{dof}$  for the solution of Eq. (19) shown in the relevant columns of Table II and may indicate that the summation method is not able to properly account for the large excited-state contamination found in  $G_P(Q^2)$  when using only the axial current. By contrast, the results obtained using the two-state method (shown in the right panel of Fig. 8) indicate good stability against the choice of including or excluding the pseudoscalar density. This observation is corroborated by the values of  $\chi^2/\text{dof}$  shown in the relevant columns of Table II. It is also worth noting that while the results from the summation method show a high sensitivity to the choice of the operator basis used in solving Eq. (19), a marked improvement in the compatibility with the results from the two-state method is observed when the pseudoscalar density is included. Since judging from their stability under the choice of operator basis, the results obtained with the two-state method appear to be more reliable, the two-state method will be the method of choice in our subsequent analysis.

In summary, the ground-state matrix elements extracted with the two-state fit method are overall consistent with the PCAC relation Eq. (9), which is a non-trivial check that excited-state contaminations have been removed, since the extraction of each term in Eq. (9) may be affected differently by excited states. By contrast, the ground-state matrix elements extracted with the summation method do not satisfy the PCAC relation, as seen from the large reduced  $\chi^2$  values in Table II; we therefore do not use the summation method for our final results, but nonetheless quote intermediate results derived from it in tables IV and V. In the future, we hope to carry out high-statistics calculations at such large source-sink separations that both methods yield ground-state matrix elements that are consistent with each other and with the PCAC relation.

## VI. CHIRAL ANALYSIS

In order to provide predictions for the physical world, it remains to extrapolate our lattice results obtained at unphysical values of the light quark masses to the physical pion mass and the continuum limit. The standard approach to this problem is to take the values of the observables of interest ( $g_A$  and the axial charge radius in our

TABLE III. The low-energy constants relevant to the EFT description of the nucleon axial-vector form factors [9], with the values used in the fits to our lattice data. Quantities with a circle on top denote values in the chiral limit; in the case of the nucleon mass, higher-order effects are accounted for by using either the physical nucleon mass or the measured value on each lattice ensemble.

Interaction	Low-energy constant	Value and role in the fit
$\mathcal{L}^{(2)}$	$F$	$F_\pi^{\text{exp}} = 92.2 \text{ MeV}$
	$m_\pi^2$	Lattice input
$\mathcal{L}_A^{\text{eff}}$	$M_A$	$M_{a_1} = 1.23 \text{ GeV}$ (Ref. [1])
$\mathcal{L}_{\pi N}^{(1)}$	$F_G$	Fit parameter contributing to $\langle r_A^2 \rangle$ and $G_{A,P}$
	$\overset{\circ}{m}_N$	Lattice input or $m_N^{\text{phys}} = 938.3 \text{ MeV}$
	$\overset{\circ}{g}_A$	Fit parameter contributing to $G_A$ and $G_P$
$\mathcal{L}_{\pi N}^{(2)}$	$c_3$	$c_3 = -4.2/m_N^{\text{phys}}$ (Ref. [71]) or $c_3 = -5.61 \text{ GeV}^{-1}$ (Refs. [72, 73])
	$c_4$	$c_4 = 2.3/m_N^{\text{phys}}$ (Ref. [71]) or $c_4 = 4.26 \text{ GeV}^{-1}$ (Refs. [72, 73])
$\mathcal{L}_{\pi N}^{(3)}$	$d_{16}$	Fit parameter contributing to $G_A$ and $G_P$
	$d_{18}$	Fit parameter contributing to $G_P$
	$d_{22}$	Fit parameter contributing to $\langle r_A^2 \rangle$ and $G_{A,P}$

case) as determined on each ensemble, and to extrapolate them to the physical point using formulae taken from, or inspired by, Chiral Perturbation Theory (ChPT).

### A. Combined fit in chiral effective theory

One possible approach that can be applied here is very similar to that performed in our paper [44] on the electromagnetic form factors of the nucleon: we perform a fit of the dependence of the form factors  $G_A$  and  $G_P$  on both the pion mass and the squared momentum transfer  $Q^2$  to the expressions of baryonic effective field theory (EFT), including explicit axial vector degrees of freedom [9]. The main motivation for this ansatz is that the inclusion of the axial vector meson extends the range in  $Q^2$  for which a phenomenologically good description of the form factor data is achieved [9]. This increases the number of points amenable to a simultaneous fit to the  $Q^2$  and pion mass dependence of the form factors  $G_A$  and  $G_P$ . From such a fit we extract the LECs and subsequently use the so obtained values at the physical pion mass to quote the extrapolated result for our data. This approach avoids the two-step procedure of first extracting the form factors and derived quantities using a dipole fit or a  $z$ -expansion analysis, before applying a chiral extrapolation. It also has the potential advantage that values are obtained for low-energy constants that can be used in describing other observables.

The full analytic form of the ansatz is quite lengthy; it can be found in [9]. While we do not reproduce it in its full length here, the contributions of the fit parameters to  $G_A(q^2)$  and  $G_P(q^2)$  are simple to write down,

$$G_A^{\text{EFT}}(q^2) = \overset{\circ}{g}_A + 4m_\pi^2 d_{16} - d_{22} q^2 - 8F_G \frac{q^2}{q^2 - M_A^2} + \mathcal{O}(\hbar), \quad (27)$$

$$G_P^{\text{EFT}}(q^2) = 4m_N^2 d_{22} + \frac{4m_N^2}{q^2 - m_\pi^2} \left( -\overset{\circ}{g}_A + 2m_\pi^2 (d_{18} - 2d_{16}) + \mathcal{O}(\hbar) \right) + 32 \frac{F_G m_N^2}{q^2 - M_A^2} + \mathcal{O}(\hbar), \quad (28)$$

where  $\mathcal{O}(\hbar)$  indicates terms of at least one-loop order. The fitted low-energy constants are  $\overset{\circ}{g}_A$ ,  $d_{16}$ ,  $d_{18}$ ,  $d_{22}$  and  $F_G$ , as summarized in Table III. The low-energy constants  $c_3$  and  $c_4$ , and the mass  $M_A$  of the axial vector meson are

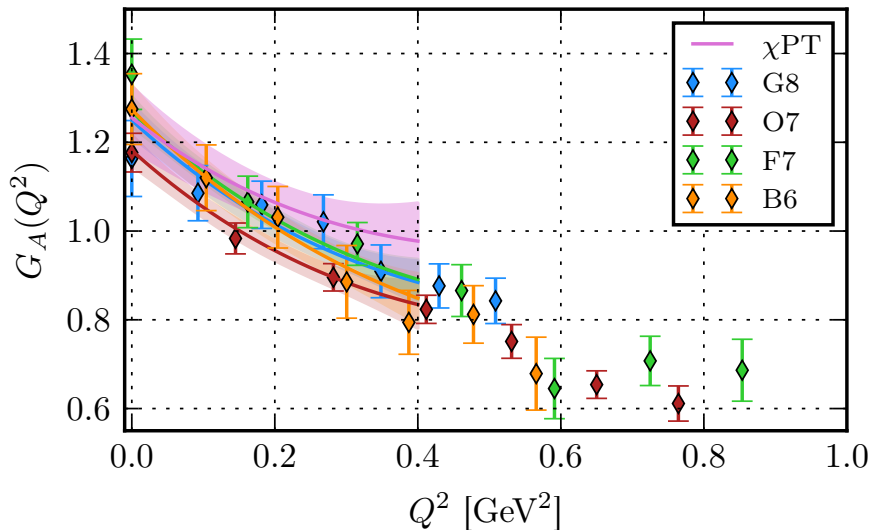


FIG. 9. Our results for the axial form factor  $G_A(Q^2)$  of the nucleon, with the chiral fit and its extrapolation to the physical point. The band in the same colour as the data point for each ensemble represents the result of inserting into the fit function the pion mass and lattice spacing of that ensemble, and the purple band labelled “ $\chi$ PT” represents the fit function in the continuum limit at the physical pion mass.

set to their phenomenological values [71], while for the nucleon mass its measured value on each ensemble is used. A pion-mass cut of  $m_\pi \leq 280$  MeV is applied to the fits, which thereby only include four ensembles, as well as a momentum cut of  $Q^2 \leq 0.4$  GeV<sup>2</sup>. The reason for the reduction in the  $m_\pi$  fit range is that we obtained values for the  $\chi^2/\text{d.o.f}$  of about 4-5 with the less restrictive choice of  $m_\pi < 335$  MeV made in the next subsection. We perform a simultaneous fit to both  $G_A(Q^2)$  and  $G_P(Q^2)$  using a fit function accounting for the leading discretisation effects,

$$G_{A,P}(Q^2) = G_{A,P}^{\text{EFT}}(Q^2, m_\pi) + e_1^{A,P} a^2 + e_2^{A,P} Q^2 a^2. \quad (29)$$

In order to estimate the influence of various systematic effects, we also perform a number of variations on the fit by

1. neglecting discretisation effects ( $e_1^{A,P} = e_2^{A,P} = 0$ ),
2. not applying a cut in  $Q^2$ ,
3. using the physical nucleon mass on all ensembles, and
4. using different values for the low-energy constants  $c_3$  and  $c_4$ .

Examples of the standard fit are shown in figures 9 and 10, and the values for  $g_A$ ,  $\langle r_A^2 \rangle$ , and  $g_P$  resulting at the physical pion mass for the different variations are tabulated in Table IV. The shape and overall normalization of  $G_P$  in particular compares very favourably with the (limited) experimental data. The axial charge in the chiral limit tends to come out at a large value, while the obtained value of the parameter  $d_{16}$  gives an unnaturally large negative slope of  $g_A$  as a function of  $m_\pi^2$ . For this and other reasons given in section VII, we use fits to the pion-mass dependence of the axial charge and radius for our final results; these fits are presented in the next subsection. Nonetheless, we think that the effectiveness and stability of the EFT fit should be re-evaluated once more accurate data at small pion mass and virtualities becomes available.

## B. HBChPT-inspired fits

In order to enable a comparison with the standard approach, we also perform fits to the pion-mass dependence of the axial radius and the axial charge using several variants of HBChPT-inspired chiral fits. In order to determine whether our data allow for the resolution of the chiral logarithm, we fit each quantity  $\mathcal{Q}$  using the ansätze

$$\mathcal{Q}(m_\pi) = A + Bm_\pi^2, \quad (30)$$

$$\mathcal{Q}(m_\pi) = A + Bm_\pi^2 + Cm_\pi^2 \log m_\pi, \quad (31)$$



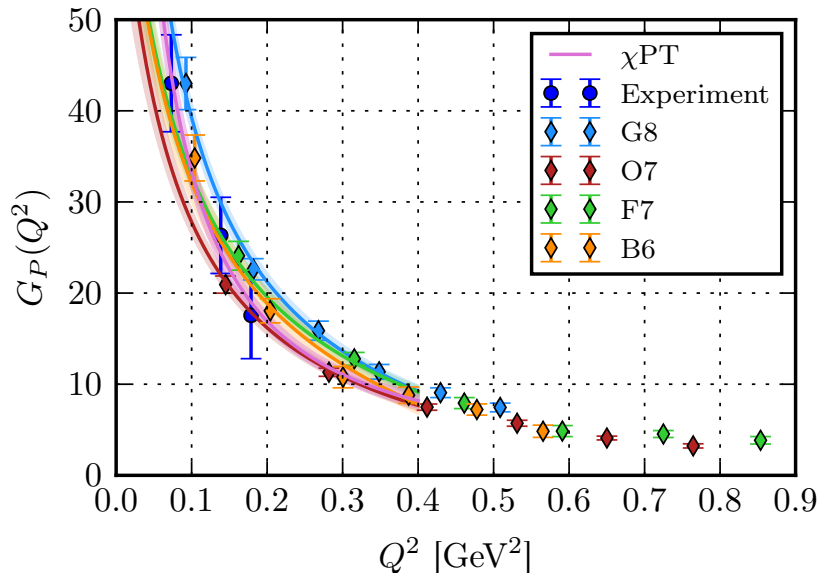


FIG. 10. Our results for the induced pseudoscalar form factor  $G_P(Q^2)$  of the nucleon, with the chiral fit and its extrapolation to the physical point. The band in the same colour as the data point for each ensemble represents the result of inserting into the fit function the pion mass and lattice spacing of that ensemble, and the purple band labelled “ $\chi$ PT” represents the fit function in the continuum limit at the physical pion mass. Also shown (blue circles) are experimental results [74], to which our prediction can be seen to compare quite favourably.

with three and two fit parameters, respectively. The linear fit (30) is applied both with (Fit A) and without (Fit B) a pion-mass cut of  $m_\pi \leq 335$  MeV<sup>4</sup> in order to check for the importance of higher-order corrections, while the fit (31) including a logarithmic term is applied over the whole pion mass range (Fit C).

In the case of the axial charge, we use a modified version of Fit C, namely

$$g_A(m_\pi) = \dot{g}_A + Bm_\pi^2 - \frac{\dot{g}_A}{8\pi^2 F^2} (1 + 2\dot{g}_A^2) m_\pi^2 \log m_\pi \quad (32)$$

with fit parameters  $\dot{g}_A$  and  $B$ , and the chiral-limit pion decay constant fixed to its phenomenological value  $F = 86$  MeV [75, 76]; a pion-mass cut of  $m_\pi \leq 335$  MeV is applied in this case. The reason is that using Eq. (31) with the coefficient of the logarithmic term left free gives implausible results in that the sign of the logarithmic term comes out positive, contrary to the ChPT result incorporated into Eq. (32). Comparing the results of the different fits (cf. Fig. 3), we conclude that our data are not precise enough to allow for a reliable resolution of the chiral logarithm, and that applying the fit form 32 amounts to imposing a trend which is not seen at all in our data. Even with Fit A, we observe that the slope of  $g_A$  as a function of  $m_\pi^2$  is only poorly constrained. In the results presented in Table V, we have assumed that the results are independent of the lattice spacing, since we already observed that no particular trend in the cutoff dependence is seen in the  $g_A$  or  $\langle r_A^2 \rangle$  data for  $m_\pi \leq 335$  MeV. For an indication of how sensitive the results are to this assumption, we quote the result of a simultaneous linear extrapolation in  $a^2$  and  $m_\pi^2$  (i.e. a three-parameter fit) of the axial charge for  $m_\pi \leq 335$  MeV: we find  $g_A = 1.236(88)$  at the physical pion mass, to be compared with  $g_A = 1.278(68)$  assuming no cutoff effects. The difference is well contained in the uncertainty estimate. At the same time, we note that the description including  $O(a^2)$  cutoff effects is overfitting the data, as witnessed by the fact that the  $\chi^2/\text{d.o.f.}$  goes up from 1.07 to 1.21 in spite of the additional fit parameter. As a further alternative, if we perform Fit A without an  $O(a^2)$  but remove the data from the coarsest lattice spacing, we obtain  $g_A = 1.278(72)$  at the physical pion mass, i.e. no change except for an insignificant increase in the statistical uncertainty.

For the axial charge radius, we find that the linear fits without a pion-mass cut do not describe our data well, whereas both the linear fits with a pion-mass cut and the fits including a logarithmic term are well compatible with our data (cf. Fig. 6).

<sup>4</sup> The ensemble N6 is included both in Fit A and in Fit B.

TABLE IV. Results for the axial charge  $g_A$ , square of the axial charge radius  $\langle r_A^2 \rangle$ , and pseudoscalar charge  $g_P$  of the nucleon from a chiral EFT fit to our lattice data. The  $\chi^2$  per degree of freedom and the number  $\nu_{\text{d.o.f.}}$  of degree of freedom are given in the last two columns. In all fits only the four most chiral ensembles G8, F7, F6 and B6 are used. The ‘‘Standard’’ fit incorporates a momentum cut  $Q^2 < 0.4 \text{ GeV}^2$ , uses the lattice nucleon mass on each ensemble, explicitly accounts for  $\mathcal{O}(a^2)$  cut-off effects and has 9 fit parameters altogether. Also shown are several variations that can be used to estimate the systematic error.

Fit variant	Method	$g_A$	$\langle r_A^2 \rangle [\text{fm}^2]$	$g_P$	$\chi_{\text{red}}^2$	$\nu_{\text{d.o.f.}}$
Standard	summation	1.255(71)	0.238(77)	8.3(5)	0.59	19
No $\mathcal{O}(a^2)$		1.318(41)	0.216(58)	8.8(3)	0.63	23
No $Q^2$ cut		1.325(48)	0.217(29)	8.8(3)	0.61	43
With $m_N^{\text{phys}}$		1.314(78)	0.217(75)	8.9(5)	1.71	19
Alternative $c_i$		1.336(71)	0.209(73)	8.8(5)	0.47	19
Standard	two-state	1.382(91)	0.246(92)	9.0(7)	0.50	19
No $\mathcal{O}(a^2)$		1.418(66)	0.202(69)	9.4(4)	0.61	23
No $Q^2$ cut		1.427(70)	0.287(36)	9.4(5)	0.50	43
With $m_N^{\text{phys}}$		1.399(98)	0.214(92)	9.4(7)	1.25	19
Alternative $c_i$		1.478(91)	0.222(86)	9.7(7)	0.29	19

TABLE V. Summary of the results of chiral fits using a linear fit form with a pion-mass cut of  $m_\pi \leq 335 \text{ MeV}$  (Fit A) or no pion-mass cut (Fit B), or a ChPT-inspired fit form with a logarithmic term (Fit C). In the case of  $g_A$ , Fit C uses Eq. (32) with a pion mass cut of  $m_\pi \leq 335 \text{ MeV}$ ; otherwise, Fit C uses Eq. (31) and data at all pion masses.

	$g_A$	$\langle r_A^2 \rangle [\text{fm}^2]$	$g_P$
Two-state fit			
Fit A	1.278(68)	0.360(36)	7.7(1.8)
Fit B	1.191(27)	0.271(12)	8.5(1.5)
Fit C	1.186(56)	0.440(47)	5.7(2.1)
Summation method			
Fit A	1.208(69)	0.279(26)	8.2(1.6)
Fit B	1.200(34)	0.242(12)	8.0(1.5)
Fit C	1.138(59)	0.330(39)	7.6(1.9)

The pseudoscalar coupling defined by Eq. (5) is not readily accessible from our results for  $G_P$  because its  $Q^2$  and  $m_\pi^2$  dependence is strong, due to the pion pole. However, observing that the pion-nucleon form factor  $G_{\pi N}(Q^2)$  depends less strongly on  $Q^2$  and  $m_\pi^2$ , we proceed as follows. First, the form factor  $G_{\pi N}(Q^2)$  is determined on every ensemble at the available  $Q^2$  values by taking the appropriate linear combination of  $G_A(Q^2)$  and  $G_P(Q^2)$ ; see Eqs. (8) and (9). Then a monopole fit is performed (see Fig. 11),

$$G_{\pi N}(Q^2) = \frac{C}{\Lambda^2 + Q^2}, \quad (33)$$

which allows us to extract  $G_{\pi N}(Q_*^2)$  on every ensemble. The latter is then chirally (and continuum) extrapolated to the physical point; see Fig. 12. We use the already determined values of  $g_A$  and  $\langle r_A^2 \rangle$  at the physical pion mass to obtain  $G_A(Q_*^2)$  via (3), since  $Q_*^2$  is very small. Finally, taking the appropriate linear combination of  $G_A(Q_*^2)$  and  $G_{\pi N}(Q_*^2)$  yields  $g_P$  at the physical pion mass. The momentum-transfer dependence (33) of  $G_{\pi N}$  was proposed in [9]; it describes the lattice data well, as can be seen from Fig. 11. We find that this dependence is very mild, reflecting the fact that the pion pole describes the bulk of the  $Q^2$  dependence of  $F_P(Q^2)$ . Since  $Q_*^2$  is small on hadronic scales

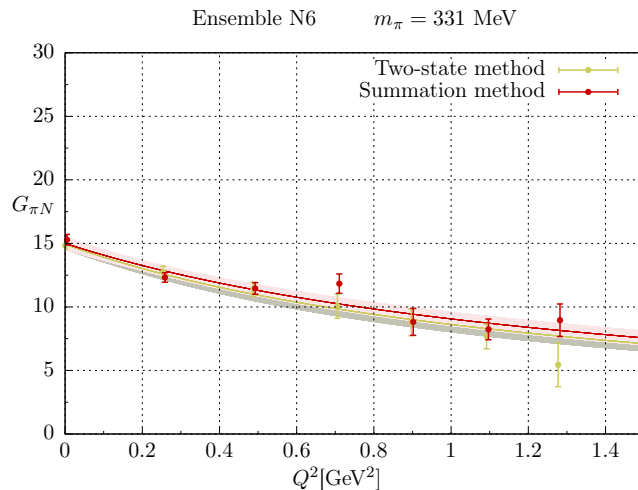


FIG. 11. The form factor  $G_{\pi N}(Q^2)$  on ensemble N6, parameterized by the monopole ansatz (33), for the summation and the two-state-fit methods.

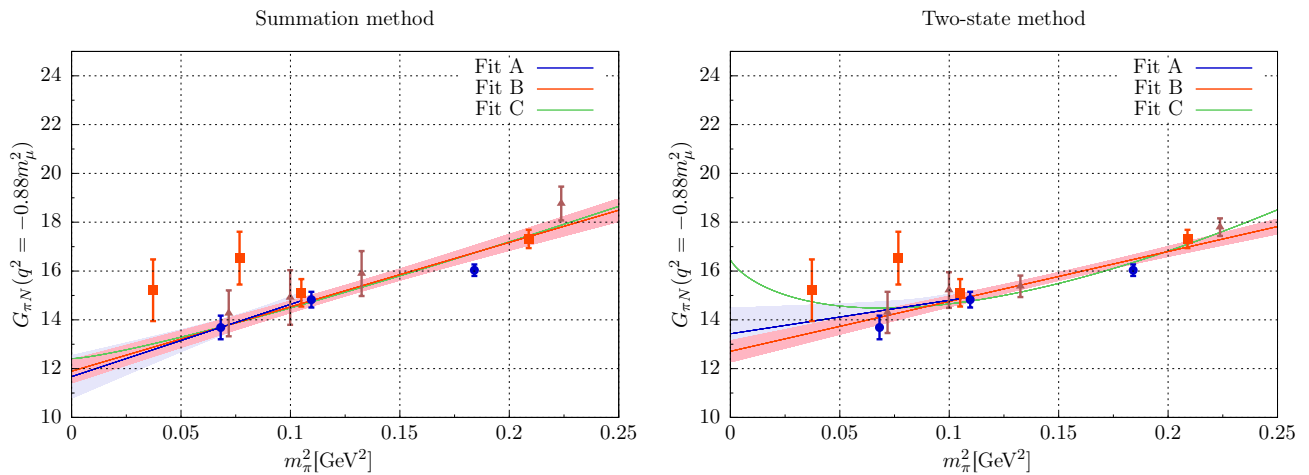


FIG. 12. Chiral extrapolation of  $G_{\pi N}(Q_*^2)$  for the summation method (left) and the two-state-fit method (right panel). Triangles, squares and circles correspond to increasingly fine lattice spacings. Fit A is a linear fit with a pion-mass cut  $m_\pi \leq 335$  MeV, Fit B is a linear fit with no pion-mass cut, and Fit C incorporates a logarithmic term via eqn. (31).

and Eq. 9 implies  $G_{\pi N}(0) = \frac{M_N g_A}{F_\pi}$ , the sensitivity of  $G_{\pi N}(Q_*^2)$  to the specific form of the ansatz (33) is weak.

A summary of our results for  $g_A$ ,  $\langle r_A^2 \rangle$ , and  $g_P$  can be found in Table V.

## VII. DISCUSSION AND CONCLUSION

As discussed above, we use in our main analysis the form factors extracted with the two-state fit in order to remove excited-state contributions. We include the pseudoscalar density in our analysis, as its matrix elements are overall compatible with those of the axial current via the PCAC relation and tend to increase the precision of the calculation.

As for the chiral extrapolation, we have performed simultaneous fits to the pion-mass and momentum transfer dependence, as well as the more widely used two-step procedure of first extracting the small- $Q^2$  observables and then chirally extrapolating them. A disadvantage of the simultaneous chiral fits to  $G_A$  and  $G_P$  is that it is intrinsically a small- $Q^2$  expansion, and the paucity of the lattice data in this region, as compared to previous lattice calculations of the pion electromagnetic form factor [77], adversely affects the stability of the fits. Empirically, we find that the fitted values of the low-energy constants  $d_{16}$  and  $d_{18}$  come out large and poorly constrained, casting some doubt on whether convergence is under control. Secondly, in the chiral expansion the leading correction to the (pion-mass independent) leading-order value for the slope of the axial form factor happens to vanish; this implies that the fit ansatz imposes

a pion-mass dependence of the axial radius which is completely dominated by the pion-mass dependence of the axial charge (see Eq. (4)). Third, the chiral logarithm predicted in the pion-mass dependence of the axial charge is not seen in the data (see Fig. 3). For these reasons, unlike in our study of the vector form factors [44], we prefer in the present study to quote as final results those obtained with the more conventional procedure of first extracting the axial charge and radius and  $g_P$  on each ensemble, followed by a chiral extrapolation. Nonetheless, we have presented the effective field theory analysis because this type of combined fits may be useful in future calculations involving more accurate data in the very chiral and low-momentum regime.

For our final numbers, we choose to quote the result of applying a linear fit with a pion-mass cut of  $m_\pi \leq 335$  MeV (Fit A) to the data obtained from the two-state fit method. We estimate the systematic error from the chiral extrapolation by taking the difference between the fits with and without a pion-mass cut (Fits A and B) as a one-sided systematic error; where the fit including a logarithmic term (Fit C) lies on the other side of our central value, we include the corresponding difference into an asymmetric two-sided systematic error. We note that the results from the summation method are also covered by the resulting error bars, and that our results are therefore not sensitive to excited-state effects at this level of accuracy. We thus finally obtain

$$\begin{aligned} g_A &= 1.278 \pm 0.068^{+0.000}_{-0.087}, \\ \langle r_A^2 \rangle &= 0.360 \pm 0.036^{+0.080}_{-0.088} \text{ fm}^2, \\ g_P &= 7.7 \pm 1.8^{+0.8}_{-2.0}, \end{aligned} \quad (34)$$

where the first error is statistical and the second systematic. All three results are compatible with the phenomenological values of these quantities:  $g_A = 1.2723(23)$  (the Particle Data Group average of neutron  $\beta$  decay data [1]),  $\langle r_A^2 \rangle = 0.444(18)\text{fm}^2$  (from a dipole fit to neutrino scattering data, see [8] for a review and other determinations of the axial charge radius), and  $g_P = 8.06(55)$  (from the MuCap experiment [13, 14]).

Several other lattice calculations of the axial charge have appeared recently [21, 23, 24, 26, 28, 34–38]. In particular, the values obtained in [21, 23, 24, 26, 28] at the physical pion mass also agree with the phenomenological value, while the calculation in [37] yields a slightly lower value. Most of them quote a rather more precise result, however the precision depends strongly on the source-sink separations and the ranges of pion masses used in the chiral extrapolation. For example, as compared to our earlier publication on the axial charge [18], the final quoted error has changed little, but the present chiral extrapolation is based on the interval  $190 \leq m_\pi/\text{MeV} \leq 335$ , rather than on  $270 \leq m_\pi/\text{MeV} \leq 540$ . This comparison also illustrates the increasing computational cost of determining nucleon structure observables as the pion mass is reduced.

In order to remove the effect of applying different procedures for the chiral extrapolations, in Fig. 13 we compare recent lattice results for the axial charge at  $m_\pi \simeq 300$  MeV obtained on reasonably large and fine lattices satisfying  $m_\pi L > 4$  and  $a < 0.095$  fm. Since the range of source-sink separations used in the calculations is one of the main quality criteria, we indicate this range by a horizontal segment in Fig. 13. Within the uncertainties of the comparison, we observe a consistent picture. Most results cluster between 1.20 and 1.24, while the central value of our result on ensemble N6 lies somewhat lower. While the available data does not allow one to identify a specific trend as a function of the flavor content of the calculations or on the lattice spacing, future continuum-extrapolated results would allow for a more controlled comparison. Finally, we remark that the challenge for the future will be to maintain or improve the statistical precision while extracting the axial charge exclusively from source-sink separations exceeding 1.5 fm.

To a more limited extent, we can also compare our result for the axial radius to other lattice determinations. Again, we favor performing the comparison at a fixed pion mass of about 300 MeV. In extracting the radius, the precise fit form used to describe the axial form factor plays an important role, both for the central value and the achieved statistical precision. Using a dipole fit, Ref. [38] obtains  $\langle r_A^2 \rangle = 0.242(29) \text{ fm}^2$  for  $m_\pi = 320$  MeV on their ensemble a06m310; with a dipole fit, our result  $\langle r_A^2 \rangle = 0.239(21) \text{ fm}^2$  for  $m_\pi = 331$  MeV on ensemble N6 agrees very well. Also, at  $m_\pi = 317$  MeV Ref. [36] obtains 0.213(15), where we have added the errors in quadrature, from a  $z$ -expansion fit with five terms and Gaussian priors starting at the third term. These recent results are thus in good agreement.

Probably the most critical step in the presented lattice calculation is the extraction of the ground-state matrix elements from the correlation functions. We have used two theoretically well motivated methods, the summation and two-state method described in section III, in order to perform this task. For the axial form factor at  $Q^2 \lesssim 0.5 \text{ GeV}^2$ , we observe good agreement between the two methods, adding confidence in the results for  $g_A$  and  $\langle r_A^2 \rangle$ . The situation for the form factors containing the pion pole ( $G_P$ ,  $F_P$ ) is less satisfactory, in the sense that only the two-state-fit method led to ground-state matrix elements consistent with the PCAC relation Eq. (9). It is for that reason that we chose the two-state-fit method to present our final results. In the future, by performing calculations at larger source-sink separations, we hope to benefit from more cross-checks, as in the case of the axial form factor. At the same time, the corrections to the mid-point values of the ratios  $R.(t = t_s/2, t_s)$ , induced by the summation or two-state-fit method in extracting the ground-state matrix elements, would be reduced.

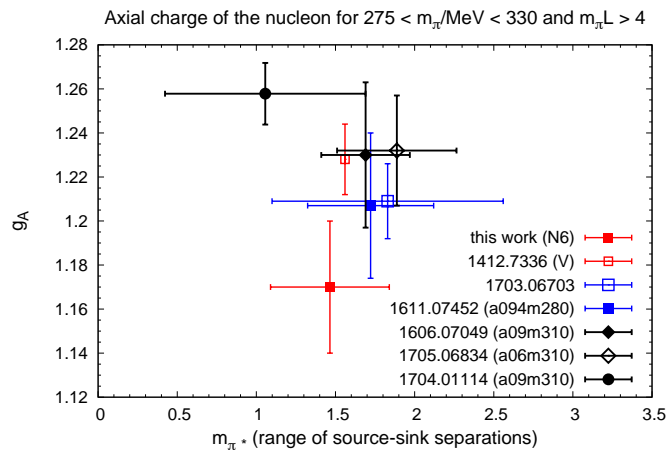


FIG. 13. Comparison of select recent lattice results for the axial charge of the nucleon at  $m_\pi \simeq 300$  MeV. Attached to each data point, a horizontal line indicates the range of source-sink separations used in the calculation. The caption indicates the arXiv number of the respective publications, with the relevant lattice ensemble given in brackets. Red points correspond to two-flavor, blue points to 2+1 flavor and black points to 2+1+1 flavor calculations. Square data points correspond to an  $O(a)$  improved Wilson fermion action; the other data points come from a mixed-action approach with staggered sea quarks.

In summary, we have performed a two-flavour lattice QCD calculation of the isovector axial and induced pseudoscalar nucleon form factors. We have consistently applied the  $\mathcal{O}(a)$  improvement program and observe no significant cutoff effect on the low- $Q^2$  observables at pion masses below 350 MeV. We have made use of the pseudoscalar density. Its form factor is related to the axial and induced pseudoscalar form factor by the PCAC relation, and thus it provides both a cross-check of the calculation and a slight increase in precision. The axial charge, the axial radius and the pseudoscalar coupling we obtained are in agreement with experiment.

In the near future, we plan to improve on our calculation by using 2 + 1-flavour ensembles (i.e. containing the sea-quark effects of both the light and strange quarks), by increasing the statistics by an order of magnitude and by going to larger source-sink separations. A preliminary account of the results was presented at the Lattice 2016 conference [78]. The lessons learnt from the analysis applied here will be beneficial in this endeavour.

## ACKNOWLEDGMENTS

We are grateful to our colleagues within the CLS initiative for sharing ensembles. We have used the LoopTools library [79] in the numerical evaluation of the EFT amplitudes [9].

Our calculations were performed on the “Wilson” HPC Cluster at the Institute for Nuclear Physics, University of Mainz, and on the “Clover” HPC Cluster at the Helmholtz Institute Mainz. We are grateful to Christian Seiwert for technical support. We are also grateful for computer time allocated to project HMZ21 on the BG/Q “JUQUEEN” computer at NIC, Jülich. This work was granted access to the HPC resources of the Gauss Center for Supercomputing at Forschungszentrum Jülich, Germany, made available within the Distributed European Computing Initiative by the PRACE-2IP, receiving funding from the European Community’s Seventh Framework Programme (FP7/2007-2013) under Grant No. RI-283493.

This work was supported by the Deutsche Forschungsgemeinschaft (DFG) in the SFB 443 and SFB 1044, and by the Rhineland-Palatinate Research Initiative. M.D.M. was partially supported by the Danish National Research Foundation under Grant No. DNRF:90. B.J. was supported by the Schweizerischer Nationalfonds (SNF) under grant 200020-162515. P.M.J. acknowledges support from the Department of Theoretical Physics, TIFR. T.D.R. was supported by DFG grant HA4470/3-1.

## Appendix A: Form factor values

In Tables VI–XVI we give all of our results for the iso-vector axial form factors  $G_A$  and  $G_P$  of the nucleon at all values of  $Q^2$  measured on each ensemble. Listed in each case are the values obtained using the summation method

and an explicit two-state fit (cf. the main text for details). The statistical errors on each data point are quoted in parentheses following the central value.

TABLE VI. A3 ensemble ( $a = 0.079$  fm,  $m_\pi = 473$  MeV,  $t_s/a \in \{10, 12, 14, 16\}$ ): The axial, induced pseudoscalar, and pion-nucleon pseudoscalar form factors at all  $Q^2$  values for all extraction methods.

A3	$G_A$		$G_P$		$G_{\pi N}$	
	Two-state	Summation	Two-state	Summation	Two-state	Summation
$Q^2$ [GeV <sup>2</sup> ]						
0.0	1.222 (0.024)	1.276 (0.049)	-	-	18.03 (0.356)	18.83 (0.717)
0.230	1.057 (0.025)	1.052 (0.041)	17.47 (0.664)	16.88 (1.125)	15.43 (0.413)	15.84 (0.637)
0.448	0.922 (0.026)	0.919 (0.040)	9.829 (0.345)	10.14 (0.568)	14.63 (0.598)	13.68 (0.805)
0.655	0.790 (0.033)	0.755 (0.054)	6.222 (0.338)	6.034 (0.575)	14.04 (0.833)	12.99 (1.313)
0.823	0.680 (0.043)	0.597 (0.074)	4.656 (0.381)	4.057 (0.678)	11.37 (1.011)	10.27 (1.812)
1.013	0.675 (0.051)	0.612 (0.084)	3.955 (0.323)	3.722 (0.561)	11.13 (1.080)	8.616 (1.793)
1.196	0.585 (0.067)	0.494 (0.115)	2.858 (0.357)	2.466 (0.649)	11.75 (1.694)	9.133 (2.869)

TABLE VII. A4 ensemble ( $a = 0.079$  fm,  $m_\pi = 364$  MeV,  $t_s/a \in \{10, 12, 14, 16\}$ ): The axial, induced pseudoscalar, and pion-nucleon pseudoscalar form factors at all  $Q^2$  values for all extraction methods.

A4	$G_A$		$G_P$		$G_{\pi N}$	
	Two-state	Summation	Two-state	Summation	Two-state	Summation
$Q^2$ [GeV <sup>2</sup> ]						
0.0	1.170 (0.033)	1.199 (0.080)	-	-	15.42 (0.430)	15.80 (1.054)
0.229	1.022 (0.038)	0.985 (0.042)	16.41 (1.069)	15.74 (1.135)	14.04 (0.826)	13.64 (0.914)
0.442	0.978 (0.054)	0.984 (0.074)	9.304 (0.541)	9.258 (0.771)	16.35 (2.337)	16.90 (2.163)
0.643	0.823 (0.056)	0.817 (0.074)	6.064 (0.492)	5.812 (0.670)	12.92 (1.242)	14.51 (2.047)
0.805	0.926 (0.164)	0.822 (0.161)	6.017 (1.184)	5.299 (1.133)	10.39 (1.894)	9.725 (2.688)
0.987	0.674 (0.088)	0.546 (0.103)	3.429 (0.486)	2.857 (0.584)	11.63 (1.648)	7.992 (2.287)
1.162	0.575 (0.106)	0.359 (0.159)	2.537 (0.509)	1.830 (0.712)	10.18 (1.893)	0.205 (4.267)

TABLE VIII. A5 ensemble ( $a = 0.079$  fm,  $m_\pi = 316$  MeV,  $t_s/a \in \{10, 12, 14, 16\}$ ): The axial, induced pseudoscalar, and pion-nucleon pseudoscalar form factors at all  $Q^2$  values for all extraction methods.

A5	$G_A$		$G_P$		$G_{\pi N}$	
	Two-state	Summation	Two-state	Summation	Two-state	Summation
$Q^2$ [GeV <sup>2</sup> ]						
0.0	1.208 (0.058)	1.238 (0.092)	-	-	15.27 (0.738)	15.65 (1.165)
0.228	1.018 (0.069)	0.987 (0.064)	16.96 (1.541)	16.90 (1.462)	12.88 (0.941)	11.72 (1.003)
0.440	0.853 (0.072)	0.869 (0.078)	8.433 (0.822)	8.662 (0.934)	11.94 (1.111)	11.74 (1.056)
0.638	0.620 (0.088)	0.642 (0.099)	4.386 (0.739)	4.245 (0.816)	10.13 (1.910)	13.71 (2.561)
0.797	0.451 (0.143)	0.424 (0.162)	2.343 (0.946)	2.067 (1.105)	12.45 (2.555)	13.94 (3.250)
0.977	0.410 (0.094)	0.357 (0.115)	2.075 (0.485)	1.775 (0.616)	5.331 (2.239)	5.396 (2.410)
1.148	0.389 (0.149)	0.376 (0.187)	1.731 (0.641)	1.451 (0.813)	4.088 (5.517)	11.20 (5.863)

TABLE IX. B6 ensemble ( $a = 0.079$  fm,  $m_\pi = 268$  MeV,  $t_s/a \in \{10, 12, 14, 16\}$ ): The axial, induced pseudoscalar, and pion-nucleon pseudoscalar form factors at all  $Q^2$  values for all extraction methods.

B6	$G_A$		$G_P$		$G_{\pi N}$	
	Two-state	Summation	Two-state	Summation	Two-state	Summation
$Q^2[\text{GeV}^2]$						
0.0	1.214 (0.065)	1.275 (0.080)	-	-	14.56 (0.781)	15.29 (0.957)
0.104	1.158 (0.095)	1.120 (0.074)	35.15 (3.090)	34.82 (2.519)	12.16 (1.285)	11.26 (0.986)
0.204	1.053 (0.094)	1.031 (0.069)	18.38 (1.807)	18.06 (1.322)	13.36 (1.441)	12.99 (1.084)
0.301	0.894 (0.112)	0.886 (0.082)	11.44 (1.549)	10.78 (1.173)	12.14 (2.959)	14.13 (1.857)
0.387	0.830 (0.096)	0.794 (0.072)	9.049 (1.142)	8.792 (0.898)	9.013 (1.865)	7.812 (1.537)
0.478	0.877 (0.092)	0.812 (0.065)	7.807 (0.833)	7.222 (0.614)	10.87 (2.163)	10.16 (1.061)
0.566	0.743 (0.119)	0.679 (0.082)	5.606 (0.843)	4.837 (0.671)	10.44 (5.042)	13.06 (2.402)

TABLE X. E5 ensemble ( $a = 0.063$  fm,  $m_\pi = 457$  MeV,  $t_s/a \in \{11, 13, 15, 17\}$ ): The axial, induced pseudoscalar, and pion-nucleon pseudoscalar form factors at all  $Q^2$  values for all extraction methods.

E5	$G_A$		$G_P$		$G_{\pi N}$	
	Two-state	Summation	Two-state	Summation	Two-state	Summation
$Q^2[\text{GeV}^2]$						
0.0	1.174 (0.025)	1.213 (0.047)	-	-	17.54 (0.368)	18.12 (0.695)
0.357	0.958 (0.026)	0.971 (0.038)	12.85 (0.521)	13.11 (0.752)	14.47 (0.480)	14.52 (0.686)
0.685	0.741 (0.028)	0.727 (0.040)	5.680 (0.290)	5.434 (0.419)	14.76 (0.615)	15.28 (0.849)
0.991	0.621 (0.041)	0.560 (0.065)	3.644 (0.307)	3.102 (0.486)	12.67 (0.968)	13.47 (1.596)
1.236	0.575 (0.057)	0.535 (0.099)	2.816 (0.317)	2.620 (0.566)	12.27 (1.434)	11.45 (2.540)
1.511	0.491 (0.053)	0.413 (0.090)	2.064 (0.238)	1.676 (0.411)	10.08 (1.264)	9.950 (2.194)
1.772	0.455 (0.071)	0.397 (0.130)	1.627 (0.275)	1.390 (0.504)	10.93 (1.975)	10.48 (3.452)

TABLE XI. F6 ensemble ( $a = 0.063$  fm,  $m_\pi = 324$  MeV,  $t_s/a \in \{11, 13, 15, 17\}$ ): The axial, induced pseudoscalar, and pion-nucleon pseudoscalar form factors at all  $Q^2$  values for all extraction methods.

F6	$G_A$		$G_P$		$G_{\pi N}$	
	Two-state	Summation	Two-state	Summation	Two-state	Summation
$Q^2[\text{GeV}^2]$						
0.0	1.169 (0.041)	1.165 (0.055)	-	-	15.12 (0.529)	15.07 (0.712)
0.163	1.034 (0.059)	1.014 (0.048)	21.60 (1.655)	21.69 (1.397)	13.88 (0.667)	13.15 (0.577)
0.317	0.887 (0.052)	0.886 (0.045)	11.23 (0.754)	11.02 (0.676)	13.81 (0.842)	14.37 (0.660)
0.464	0.781 (0.062)	0.801 (0.056)	7.279 (0.694)	6.993 (0.599)	13.41 (1.128)	16.45 (1.159)
0.595	0.677 (0.069)	0.690 (0.066)	5.124 (0.663)	5.297 (0.661)	12.42 (1.016)	12.02 (1.061)
0.731	0.598 (0.058)	0.653 (0.055)	3.857 (0.423)	4.217 (0.393)	10.90 (0.953)	11.79 (0.932)
0.862	0.556 (0.078)	0.601 (0.076)	3.118 (0.494)	3.331 (0.479)	10.35 (1.070)	11.94 (1.265)

TABLE XII. F7 ensemble ( $a = 0.063$  fm,  $m_\pi = 277$  MeV,  $t_s/a \in \{11, 13, 15, 17\}$ ): The axial, induced pseudoscalar, and pion-nucleon pseudoscalar form factors at all  $Q^2$  values for all extraction methods.

F7	$G_A$		$G_P$		$G_{\pi N}$	
	Two-state	Summation	Two-state	Summation	Two-state	Summation
$Q^2[\text{GeV}^2]$						
0.0	1.350 (0.067)	1.353 (0.079)	-	-	16.79 (0.838)	16.83 (0.986)
0.162	1.112 (0.082)	1.066 (0.058)	23.86 (2.205)	24.10 (1.577)	14.70 (1.218)	12.63 (0.893)
0.315	0.991 (0.069)	0.971 (0.048)	13.12 (1.015)	12.78 (0.704)	13.21 (1.585)	13.21 (1.020)
0.461	0.868 (0.080)	0.866 (0.058)	8.250 (0.855)	7.930 (0.604)	12.89 (2.908)	15.16 (1.828)
0.591	0.636 (0.093)	0.645 (0.068)	4.608 (0.828)	4.857 (0.606)	13.06 (2.159)	11.03 (1.658)
0.725	0.708 (0.077)	0.707 (0.055)	4.516 (0.516)	4.535 (0.381)	11.51 (1.953)	11.10 (1.216)
0.854	0.661 (0.099)	0.686 (0.070)	3.676 (0.576)	3.845 (0.411)	10.22 (2.981)	9.864 (1.538)

TABLE XIII. G8 ensemble ( $a = 0.063$  fm,  $m_\pi = 193$  MeV,  $t_s/a \in \{11, 13, 15, 17\}$ ): The axial, induced pseudoscalar, and pion-nucleon pseudoscalar form factors at all  $Q^2$  values for all extraction methods.

G8	$G_A$		$G_P$		$G_{\pi N}$	
	Two-state	Summation	Two-state	Summation	Two-state	Summation
$Q^2[\text{GeV}^2]$						
0.0	1.252 (0.109)	1.163 (0.086)	-	-	14.93 (1.302)	13.87 (1.020)
0.092	1.178 (0.136)	1.085 (0.062)	43.19 (6.346)	43.00 (2.867)	14.79 (1.464)	11.11 (0.713)
0.182	1.138 (0.119)	1.059 (0.053)	26.68 (2.547)	22.61 (1.167)	9.900 (2.976)	15.01 (1.245)
0.268	1.060 (0.133)	1.021 (0.061)	17.90 (2.238)	15.87 (1.048)	7.183 (3.578)	14.26 (1.346)
0.348	0.955 (0.130)	0.909 (0.059)	11.49 (1.760)	11.36 (0.805)	16.24 (1.973)	11.72 (0.984)
0.430	0.854 (0.109)	0.876 (0.050)	9.013 (1.155)	9.068 (0.534)	8.564 (1.891)	11.20 (0.835)
0.509	0.776 (0.113)	0.843 (0.051)	7.059 (1.048)	7.449 (0.478)	6.507 (2.159)	11.07 (0.816)

TABLE XIV. N5 ensemble ( $a = 0.050$  fm,  $m_\pi = 429$  MeV,  $t_s/a \in \{13, 16, 19, 22\}$ ): The axial, induced pseudoscalar, and pion-nucleon pseudoscalar form factors at all  $Q^2$  values for all extraction methods.

N5	$G_A$		$G_P$		$G_{\pi N}$	
	Two-state	Summation	Two-state	Summation	Two-state	Summation
$Q^2[\text{GeV}^2]$						
0.0	1.152 (0.016)	1.179 (0.027)	-	-	16.18 (0.230)	16.55 (0.372)
0.256	0.982 (0.020)	0.992 (0.022)	15.24 (0.459)	15.42 (0.499)	13.57 (0.331)	13.66 (0.380)
0.494	0.845 (0.018)	0.874 (0.021)	8.193 (0.207)	8.513 (0.243)	12.63 (0.418)	12.96 (0.416)
0.719	0.745 (0.024)	0.796 (0.028)	5.393 (0.197)	5.608 (0.237)	11.71 (0.668)	13.62 (0.693)
0.918	0.648 (0.035)	0.682 (0.041)	3.910 (0.237)	4.091 (0.290)	9.718 (0.696)	10.53 (0.932)
1.122	0.566 (0.031)	0.614 (0.039)	2.836 (0.164)	3.113 (0.214)	9.377 (0.644)	9.622 (0.708)
1.317	0.532 (0.038)	0.582 (0.051)	2.343 (0.169)	2.538 (0.242)	8.522 (1.113)	9.934 (1.040)

TABLE XV. N6 ensemble ( $a = 0.050$  fm,  $m_\pi = 331$  MeV,  $t_s/a \in \{13, 16, 19, 22, 25, 28\}$ ): The axial, induced pseudoscalar, and pion-nucleon pseudoscalar form factors at all  $Q^2$  values for all extraction methods.

N6	$G_A$		$G_P$		$G_{\pi N}$	
	Two-state	Summation	Two-state	Summation	Two-state	Summation
$Q^2[\text{GeV}^2]$						
0.0	1.171 (0.025)	1.206 (0.033)	-	-	14.84 (0.317)	15.29 (0.415)
0.254	0.968 (0.030)	0.981 (0.024)	14.39 (0.612)	14.90 (0.486)	12.76 (0.444)	12.32 (0.375)
0.487	0.785 (0.027)	0.827 (0.023)	6.996 (0.288)	7.459 (0.246)	11.38 (0.565)	11.45 (0.452)
0.705	0.604 (0.037)	0.697 (0.033)	3.877 (0.284)	4.454 (0.256)	10.07 (0.961)	11.83 (0.763)
0.897	0.613 (0.054)	0.700 (0.049)	3.296 (0.315)	3.827 (0.288)	8.780 (1.040)	8.824 (1.060)
1.092	0.472 (0.043)	0.530 (0.039)	2.098 (0.202)	2.367 (0.192)	7.681 (0.975)	8.233 (0.818)
1.277	0.344 (0.056)	0.453 (0.053)	1.333 (0.220)	1.708 (0.222)	5.444 (1.721)	8.951 (1.281)

TABLE XVI. O7 ensemble ( $a = 0.050$  fm,  $m_\pi = 261$  MeV,  $t_s/a \in \{13, 16, 19, 22\}$ ): The axial, induced pseudoscalar, and pion-nucleon pseudoscalar form factors at all  $Q^2$  values for all extraction methods.

O7	$G_A$		$G_P$		$G_{\pi N}$	
	Two-state	Summation	Two-state	Summation	Two-state	Summation
$Q^2[\text{GeV}^2]$						
0.0	1.184 (0.040)	1.177 (0.044)	-	-	13.70 (0.468)	13.61 (0.504)
0.145	0.979 (0.058)	0.983 (0.035)	19.94 (1.577)	20.93 (0.944)	12.55 (0.665)	11.57 (0.414)
0.282	0.846 (0.051)	0.896 (0.031)	10.74 (0.713)	11.31 (0.448)	10.94 (0.871)	11.81 (0.469)
0.412	0.743 (0.051)	0.824 (0.032)	7.265 (0.531)	7.486 (0.341)	7.250 (1.286)	12.20 (0.670)
0.531	0.668 (0.063)	0.751 (0.038)	4.981 (0.533)	5.717 (0.326)	9.084 (1.066)	8.901 (0.724)
0.650	0.510 (0.052)	0.654 (0.031)	3.052 (0.341)	4.095 (0.208)	9.321 (0.888)	8.801 (0.582)
0.764	0.455 (0.060)	0.611 (0.040)	2.486 (0.330)	3.231 (0.229)	5.578 (1.578)	10.11 (0.730)



TABLE XVII. Results for the squared axial radius and the coupling  $g_P$  on the eleven lattice ensembles, obtained either with the summation method or the two-state fit.

	Two-state fit		Summation	
	$\langle r_A^2 \rangle$ [fm <sup>2</sup> ]	$g_P$	$\langle r_A^2 \rangle$ [fm <sup>2</sup> ]	$g_P$
A3	0.137(09)	1.93(25)	0.161(16)	1.72(61)
A4	0.134(18)	2.12(34)	0.159(29)	1.66(98)
A5	0.231(24)	3.26(61)	0.240(28)	4.82(1.18)
B6	0.224(47)	3.98(63)	0.262(37)	5.07(85)
E5	0.129(08)	2.03(25)	0.146(12)	2.89(56)
F6	0.208(21)	2.62(33)	0.192(20)	3.14(58)
F7	0.233(28)	3.76(1.12)	0.220(23)	4.29(80)
G8	0.279(65)	6.31(1.12)	0.221(39)	7.42(1.02)
N5	0.138(67)	1.85(15)	0.128(09)	2.02(31)
N6	0.198(10)	2.60(21)	0.178(10)	3.06(41)
O7	0.298(21)	3.29(30)	0.229(15)	3.46(42)

- 
- [1] **Particle Data Group** Collaboration, C. Patrignani *et al.*, Chin. Phys. **C40**, 100001 (2016).
- [2] M. Burkardt, Int. J. Mod. Phys. **A18**, 173 (2003), [arXiv:hep-ph/0207047 \[hep-ph\]](#).
- [3] A. S. Meyer, M. Betancourt, R. Gran and R. J. Hill, Phys. Rev. **D93**, 113015 (2016), [arXiv:1603.03048 \[hep-ph\]](#).
- [4] T. Kitagaki *et al.*, Phys. Rev. **D42**, 1331 (1990).
- [5] A. Bodek, S. Avvakumov, R. Bradford and H. S. Budd, J. Phys. Conf. Ser. **110**, 082004 (2008), [arXiv:0709.3538 \[hep-ex\]](#).
- [6] **A1** Collaboration, A. Liesenfeld *et al.*, Phys. Lett. **B468**, 20 (1999), [arXiv:nucl-ex/9911003 \[nucl-ex\]](#).
- [7] T. Fuchs and S. Scherer, Phys. Rev. **C68**, 055501 (2003), [arXiv:nucl-th/0303002 \[nucl-th\]](#).
- [8] V. Bernard, L. Elouadrhiri and U.-G. Meissner, J. Phys. **G28**, R1 (2002), [arXiv:hep-ph/0107088 \[hep-ph\]](#).
- [9] M. Schindler, T. Fuchs, J. Gegelia and S. Scherer, Phys.Rev. **C75**, 025202 (2007), [arXiv:nucl-th/0611083 \[nucl-th\]](#).
- [10] C. Alexandrou, G. Koutsou, T. Leontiou, J. W. Negele and A. Tsapalis, Phys. Rev. **D76**, 094511 (2007), [arXiv:0706.3011 \[hep-lat\]](#), [Erratum: Phys. Rev.D80,099901(2009)].
- [11] D. H. Wright *et al.*, Phys. Rev. **C57**, 373 (1998).
- [12] P. Winter, AIP Conf. Proc. **1441**, 537 (2012), [arXiv:1110.5090 \[nucl-ex\]](#).
- [13] **MuCap** Collaboration, V. A. Andreev *et al.*, Phys. Rev. Lett. **110**, 012504 (2013), [arXiv:1210.6545 \[nucl-ex\]](#).
- [14] **MuCap** Collaboration, V. A. Andreev *et al.*, Phys. Rev. **C91**, 055502 (2015), [arXiv:1502.00913 \[nucl-ex\]](#).
- [15] G. Martinelli and C. T. Sachrajda, Nucl. Phys. **B316**, 355 (1989).
- [16] **RBC+UKQCD** Collaboration, T. Yamazaki *et al.*, Phys. Rev. Lett. **100**, 171602 (2008), [arXiv:0801.4016 \[hep-lat\]](#).
- [17] J. R. Green *et al.*, Phys. Lett. **B734**, 290 (2014), [arXiv:1209.1687 \[hep-lat\]](#).
- [18] S. Capitani *et al.*, Phys. Rev. **D86**, 074502 (2012), [arXiv:1205.0180 \[hep-lat\]](#).
- [19] R. Horsley *et al.*, Phys. Lett. **B732**, 41 (2014), [arXiv:1302.2233 \[hep-lat\]](#).
- [20] T. Bhattacharya *et al.*, Phys. Rev. **D89**, 094502 (2014), [arXiv:1306.5435 \[hep-lat\]](#).
- [21] G. S. Bali *et al.*, Phys. Rev. **D91**, 054501 (2015), [arXiv:1412.7336 \[hep-lat\]](#).
- [22] **QCDSF/UKQCD, CSSM** Collaboration, A. J. Chambers *et al.*, Phys. Rev. **D90**, 014510 (2014), [arXiv:1405.3019 \[hep-lat\]](#).
- [23] A. Abdel-Rehim *et al.*, Phys. Rev. **D92**, 114513 (2015), [arXiv:1507.04936 \[hep-lat\]](#), [Erratum: Phys. Rev.D93,no.3,039904(2016)].
- [24] T. Bhattacharya *et al.*, Phys. Rev. **D94**, 054508 (2016), [arXiv:1606.07049 \[hep-lat\]](#).
- [25] C. Bouchard, C. C. Chang, T. Kurth, K. Orginos and A. Walker-Loud, Phys. Rev. **D96**, 014504 (2017), [arXiv:1612.06963 \[hep-lat\]](#).
- [26] B. Yoon *et al.*, Phys. Rev. **D95**, 074508 (2017), [arXiv:1611.07452 \[hep-lat\]](#).
- [27] J. Liang *et al.*, Phys. Rev. **D96**, 034519 (2017), [arXiv:1612.04388 \[hep-lat\]](#).
- [28] E. Berkowitz *et al.*, [arXiv:1704.01114 \[hep-lat\]](#).
- [29] H.-W. Lin, PoS **LATTICE2012**, 013 (2012), [arXiv:1212.6849 \[hep-lat\]](#).
- [30] G. von Hippel, T. D. Rae, E. Shintani and H. Wittig, Nucl. Phys. **B914**, 138 (2017), [arXiv:1605.00564 \[hep-lat\]](#).
- [31] T. Yamazaki *et al.*, Phys. Rev. **D79**, 114505 (2009), [arXiv:0904.2039 \[hep-lat\]](#).
- [32] **LHPC** Collaboration, J. D. Bratt *et al.*, Phys. Rev. **D82**, 094502 (2010), [arXiv:1001.3620 \[hep-lat\]](#).
- [33] **ETM** Collaboration, C. Alexandrou *et al.*, Phys. Rev. **D83**, 045010 (2011), [arXiv:1012.0857 \[hep-lat\]](#).
- [34] A. S. Meyer, R. J. Hill, A. S. Kronfeld, R. Li and J. N. Simone, PoS **LATTICE2016**, 179 (2016), [arXiv:1610.04593 \[hep-lat\]](#).
- [35] C. Alexandrou *et al.*, PoS **LATTICE2016**, 154 (2016), [arXiv:1702.00984 \[hep-lat\]](#).
- [36] J. Green *et al.*, Phys. Rev. **D95**, 114502 (2017), [arXiv:1703.06703 \[hep-lat\]](#).
- [37] C. Alexandrou *et al.*, Phys. Rev. **D96**, 054507 (2017), [arXiv:1705.03399 \[hep-lat\]](#).
- [38] R. Gupta, Y.-C. Jang, H.-W. Lin, B. Yoon and T. Bhattacharya, Phys. Rev. **D96**, 114503 (2017), [arXiv:1705.06834 \[hep-lat\]](#).
- [39] U. Mosel, Ann. Rev. Nucl. Part. Sci. **66**, 171 (2016), [arXiv:1602.00696 \[nucl-th\]](#).
- [40] D. F. Measday, Phys. Rept. **354**, 243 (2001).
- [41] M. L. Goldberger and S. B. Treiman, Phys. Rev. **110**, 1178 (1958).
- [42] M. L. Goldberger and S. B. Treiman, Phys. Rev. **111**, 354 (1958).
- [43] Y. Nambu, Phys. Rev. Lett. **4**, 380 (1960).
- [44] S. Capitani *et al.*, Phys. Rev. **D92**, 054511 (2015), [arXiv:1504.04628 \[hep-lat\]](#).
- [45] M. Lüscher, Comput. Phys. Commun. **165**, 199 (2005), [arXiv:hep-lat/0409106 \[hep-lat\]](#).
- [46] M. Lüscher, JHEP **12**, 011 (2007), [arXiv:0710.5417 \[hep-lat\]](#).
- [47] M. Marinkovic and S. Schaefer, PoS **LATTICE2010**, 031 (2010), [arXiv:1011.0911 \[hep-lat\]](#).
- [48] **ALPHA** Collaboration, K. Jansen and R. Sommer, Nucl. Phys. **B530**, 185 (1998), [arXiv:hep-lat/9803017 \[hep-lat\]](#), [Erratum: Nucl. Phys.B643,517(2002)].
- [49] S. Güsken *et al.*, Phys.Lett. **B227**, 266 (1989).
- [50] **APE** Collaboration, M. Albanese *et al.*, Phys. Lett. **B192**, 163 (1987).
- [51] G. M. von Hippel, B. Jäger, T. D. Rae and H. Wittig, JHEP **1309**, 014 (2013), [arXiv:1306.1440 \[hep-lat\]](#).
- [52] M. Della Morte, R. Sommer and S. Takeda, Phys. Lett. **B672**, 407 (2009), [arXiv:0807.1120 \[hep-lat\]](#).
- [53] M. Della Morte, R. Hoffmann and R. Sommer, JHEP **03**, 029 (2005), [arXiv:hep-lat/0503003 \[hep-lat\]](#).

- [54] S. Sint and P. Weisz, Nucl. Phys. **B502**, 251 (1997), [arXiv:hep-lat/9704001 \[hep-lat\]](#).
- [55] ETM Collaboration, C. Alexandrou *et al.*, PoS **LATTICE2008**, 139 (2008), [arXiv:0811.0724 \[hep-lat\]](#).
- [56] T. Blum, T. Izubuchi and E. Shintani, Phys. Rev. **D88**, 094503 (2013), [arXiv:1208.4349 \[hep-lat\]](#).
- [57] E. Shintani *et al.*, Phys. Rev. **D91**, 114511 (2015), [arXiv:1402.0244 \[hep-lat\]](#).
- [58] B. Jäger *et al.*, PoS **LATTICE2013**, 272 (2014), [arXiv:1311.5804 \[hep-lat\]](#).
- [59] P. M. Junnarkar *et al.*, PoS **LATTICE2014**, 150 (2015), [arXiv:1411.5828 \[hep-lat\]](#).
- [60] L. Maiani, G. Martinelli, M. L. Paciello and B. Taglienti, Nucl. Phys. **B293**, 420 (1987).
- [61] J. Bulava, M. Donnellan and R. Sommer, JHEP **01**, 140 (2012), [arXiv:1108.3774 \[hep-lat\]](#).
- [62] B. B. Brandt *et al.*, Eur. Phys. J. ST **198**, 79 (2011), [arXiv:1106.1554 \[hep-lat\]](#).
- [63] M. T. Hansen and H. B. Meyer, Nucl. Phys. **B923**, 558 (2017), [arXiv:1610.03843 \[hep-lat\]](#).
- [64] B. C. Tiburzi, Phys. Rev. **D91**, 094510 (2015), [arXiv:1503.06329 \[hep-lat\]](#).
- [65] O. Bär, Phys. Rev. **D92**, 074504 (2015), [arXiv:1503.03649 \[hep-lat\]](#).
- [66] O. Bär, Phys. Rev. **D94**, 054505 (2016), [arXiv:1606.09385 \[hep-lat\]](#).
- [67] L. A. Ahrens *et al.*, Phys. Lett. **B202**, 284 (1988).
- [68] R. J. Hill and G. Paz, Phys. Rev. **D82**, 113005 (2010), [arXiv:1008.4619 \[hep-ph\]](#).
- [69] B. Bhattacharya, R. J. Hill and G. Paz, Phys. Rev. **D84**, 073006 (2011), [arXiv:1108.0423 \[hep-ph\]](#).
- [70] J. Hua, *Determination of axial nucleon form factors in lattice QCD*, Ph.D. thesis, Joh. Gutenberg University Mainz, 2017.
- [71] T. Becher and H. Leutwyler, JHEP **06**, 017 (2001), [arXiv:hep-ph/0103263 \[hep-ph\]](#).
- [72] M. Hoferichter, J. Ruiz de Elvira, B. Kubis and U.-G. Meißner, Phys. Rept. **625**, 1 (2016), [arXiv:1510.06039 \[hep-ph\]](#).
- [73] M. Hoferichter, J. Ruiz de Elvira, B. Kubis and U.-G. Meißner, Phys. Rev. Lett. **115**, 192301 (2015), [arXiv:1507.07552 \[nucl-th\]](#).
- [74] S. Choi *et al.*, Phys. Rev. Lett. **71**, 3927 (1993).
- [75] G. Colangelo and S. Durr, Eur. Phys. J. **C33**, 543 (2004), [arXiv:hep-lat/0311023 \[hep-lat\]](#).
- [76] S. Aoki *et al.*, Eur. Phys. J. **C77**, 112 (2017), [arXiv:1607.00299 \[hep-lat\]](#).
- [77] B. B. Brandt, A. Jüttner and H. Wittig, JHEP **11**, 034 (2013), [arXiv:1306.2916 \[hep-lat\]](#).
- [78] D. Djukanovic *et al.*, PoS **LATTICE2016**, 167 (2016), [arXiv:1611.07918 \[hep-lat\]](#).
- [79] T. Hahn and M. Perez-Victoria, Comput. Phys. Commun. **118**, 153 (1999), [arXiv:hep-ph/9807565 \[hep-ph\]](#).